Additive Manufacturing 127 (2026) 105299

Contents lists available at ScienceDirect

Additive Manufacturing

journal homepage: www.elsevier.com/locate/addma

Physics-based acoustic monitoring of keyhole regime transitions in laser powder bed fusion validated by operando synchrotron X-ray imaging

Milad Hamidi Nasab [a,b,c,*,1], Rik Vaerenberg [b,c,1], Lucas Schlenger [a], Steven Van Petegem [d], Ashish Ganvir [e], Alexander Rack [f], Yunhui Chen [f,g], Antti Salminen [e], Federica Marone [h], Florian Aymanns [i], Konstantinos Gryllias [b,c], Bey Vrancken [b,c], Roland E. Logé [a]

[a] *Thermomechanical Metallurgy Laboratory – PX Group Chair, École polytechnique fédérale de Lausanne (EPFL), Neuchâtel CH-2002, Switzerland*
[b] *Department of Mechanical Engineering, KU Leuven, Leuven 3001, Belgium*
[c] *Flanders Make @ KU Leuven, Belgium*
[d] *Structure and Mechanics of Advanced Materials, Center for Photon Science, Paul Scherrer Institut, PSI, Forschungsstrasse 111, Villigen 5232, Switzerland*
[e] *Digital Manufacturing and Surface Engineering (DMS) Research Group, Mechanical Engineering, University of Turku, FI-20014, Finland*
[f] *ESRF – The European Synchrotron, Grenoble 38000, France*
[g] *School of Engineering, RMIT University, Melbourne, Australia*
[h] *Swiss Light Source, Paul Scherrer Institute, Villigen 5232, Switzerland*
[i] *EPFL Center for Imaging, École polytechnique fédérale de Lausanne (EPFL), Lausanne, Switzerland*

ARTICLE INFO

Keywords:
Laser powder bed fusion
Acoustic emission monitoring
Keyhole Dynamics
Operando Synchrotron X-ray Imaging

ABSTRACT

Additive manufacturing by Powder Bed Fusion using a Laser Beam on Metals (PBF-LB/M) enables unprecedented design freedom but remains limited by defect formation that stems from unstable melt pool dynamics. Current monitoring approaches often depend on machine learning, which can obscure the underlying physics and complicate industrial deployment. Here, a direct acoustic emission-based methodology is introduced that captures sound signatures of conduction-keyhole transitions and keyhole collapse. Using acoustic emission measurements validated by operando synchrotron X-ray imaging, a series of envelope-based indicators are established that robustly distinguish stable and unstable regimes in 316 L steel and Ti6Al4V under continuous and pulsed lasers. This physics-driven framework provides transparent, localized regime prediction, paving the way for more reliable and industrially scalable monitoring solutions in metal additive manufacturing.

1. Introduction

Laser powder bed fusion or Powder Bed Fusion - Laser Beam on Metals (PBF-LB/M) has emerged as a leading metal additive manufacturing (AM) technology capable of fabricating highly complex and precise parts by building components layer upon layer. This method offers significant advantages over conventional subtractive techniques by eliminating the need for tooling, reducing material waste, and enabling unprecedented design freedom. Industries such as aerospace, biomedical, and automotive have capitalized on these benefits, notably achieving weight reduction, enhanced productivity, and on-demand production capabilities—which together promise transformative economic and environmental impacts [1].

Typically, in the PBF-LB/M process a high-intensity laser beam selectively scans and melts thin layers of metal powder (∼15–70 μm), forming a melt pool in the order of 100 μm wide to build a 3D solid part. The interactions between the intense laser beam and the powder bed create a web of interrelated process variables whose collective impact remains only partially understood. Even when all machine settings and process parameters remain unchanged [2], the shape of the melt pool

* Correspondence to: Rue Edith Cavell 13, Uccle 1180, Belgium.
E-mail addresses: miladehamidi@gmail.com, milad.hamidinasab@epfl.ch (M. Hamidi Nasab), Rik.Vaerenberg@kuleuven.be (R. Vaerenberg), lucas.schlenger@epfl.ch (L. Schlenger), ashish.ganvir@utu.fi (A. Ganvir), alexander.rack@esrf.fr (A. Rack), yunhui.chen@rmit.edu.au (Y. Chen), antti.salminen@utu.fi (A. Salminen), federica.marone@psi.ch (F. Marone), florian.aymanns@epfl.ch (F. Aymanns), konstantinos.gryllias@kuleuven.be (K. Gryllias), bey.vrancken@kuleuven.be (B. Vrancken), roland.loge@epfl.ch (R.E. Logé).
[1] These authors contributed equally to this work.

https://doi.org/10.1016/j.addma.2026.105299
Received 4 May 2026; Received in revised form 7 July 2026; Accepted 12 July 2026
Available online 14 July 2026
2214-8604/© 2026 The Authors. Published by Elsevier B.V. This is an open access article under the CC BY license (http://creativecommons.org/licenses/by/4.0/).

can fluctuate markedly, indicating unstable conditions during building. Several factors contribute to these geometry shifts: (i) the chosen scan path and the consequent heat accumulation within each layer [3,4]; (ii) the changes in laser speed at the track's start and finish, which prolong laser exposure and lead to uneven localized energy input [5]; (iii) the presence of geometric part features, such as overhangs and thin walls, that reduce the efficiency of heat removal [6,7]; and (iv) variations in absorptivity caused by the laser's angle of incidence, resulting in nonuniform Fresnel absorption and temperature gradients along the scanning direction [8]. When these melt pool dimensions fluctuate significantly, the process may oscillate between conduction and keyhole melting modes, introducing intermittent or regular regime transitions [8].

Excessive energy input past a critical threshold [9] causes the molten metal in the laser interaction zone to vaporize rapidly, creating a recoil pressure forcing the liquid metal downward against its surface tension. This action carves out a deep, slender cavity: the keyhole [8]. Once established, the keyhole walls act like a gray body: laser light reflects multiple times within the cavity, boosting absorption and further heating [10]. At the same time, intertwined thermo-mechanical effects such as thermocapillary forces, Marangoni flows, recoil pressure spikes, and gas plasma dynamics, induce both axial swings and radial distortions in the keyhole [8,9,11,12]. Such instabilities heighten the risk of keyhole collapse and trap gas bubbles in the melt [5,13,14]. As the metal solidifies, these bubbles become fixed pores that serve as stress concentrators, ultimately impairing fatigue life and other mechanical properties of the finished part [15].

Over the past years, extensive research has been dedicated to monitoring and understanding the myriad phenomena occurring during PBF-LB/M process. A variety of in-situ sensing techniques have been employed to capture real-time process signatures including optical [16], pyrometry [17], spectroscopy [18], and Schlieren imaging [19]. However, these monitoring techniques only capture information at the surface and near-surface regions of the melt pool, coming short at providing information on the complex phenomena taking place at the bottom of the depression zone [2,20]. Therefore, acoustic monitoring has emerged as a promising alternative. As acoustic monitoring allows for capturing of information of events in the bulk of the material, previous works have shown promising results with respect to monitoring crack formation [21,22], keyhole dynamics [2], and porosity development [23]. Due to the complementarity of acoustic monitoring with other sensing techniques [24], multiple sensor fusion approaches have been proposed [25, 26]. However, the complexity of the process and the captured acoustic signals make almost all works turn to machine learning approaches [27] based on supervised [23], semi-supervised [28] or transfer learning [29]. While these ML-aided methods have shown promising results, they typically require vast datasets [30,31], can fit to non-generalizable features [32], and are very sensitive to conditions unseen in the training datasets [33] which can impede real-time process monitoring and practical industrial implementation.

In contrast to these data-driven methodologies, a smaller body of work interprets the acoustic emission through explicit physical models, including the band-energy monitoring of [34], the whistle-aeroacoustic resonator model of Sun et al. [35], and the first-principles vapor--jet-cavity oscillation framework of Liu et al. [36], the latter validated against operando synchrotron imaging of Ti6Al4V. Complementary to these interpretations, this study proposes a pure signal processing approach based on a novel amplitude modulation model of the acoustic emission (AE) signal to gain a complementary, physics-based understanding of the PBF-LB/M process. A feature common to these previous studies, and to process-mapping investigations of melting regimes more broadly [37], is that the different regimes are accessed by varying the commanded laser power and scan speed across a process map. The present work takes a deliberately different and complementary experimental route: transitions between conduction, stable keyhole, and unstable keyhole are induced under fixed commanded power and scan speed similar to previous work [2]. To validate the proposed approach, experiments were performed in beamlines at the synchrotron facilities of SLS PSI and ESRF. At these facilities, operando x-ray imaging was employed as a ground truth method to characterize melt pool dynamics and defect formation which was crucial in previous research to uncover complex melt pool dynamics [4,38,39].

Building on the constant-parameter, stochastically-induced regime-transition paradigm established in [2], and on the observation reported there that the pulse repetition frequency carries stable-versus-unstable keyhole information, this work makes three contributions. First, a phenomenological model is proposed that interprets the acoustic emission from the melt pool as amplitude-modulated vapor outflow, providing a physical basis for indicator design without reliance on machine learning or data-driven filter fitting. Second, it is demonstrated that pulsed laser operation introduces an additional amplitude modulation mechanism (the laser pulse frequency itself) that significantly improves the separation between stable and unstable keyhole regimes, which formalizes the post-hoc interpretations of the fitted filters of [2] Third, the indicators are validated on a dataset spanning two alloys (316 L and Ti6Al4V) and two laser modes (continuous and pulsed), labeled using operando synchrotron X-ray imaging at two beamline facilities, for both regime classification and melt-pool depth estimation, extending the single-alloy, pulsed-only, classification-only scope of [2]. The remainder of this paper is organized as follows: Section 2 describes the experimental setup, imaging pipeline, and the signal processing methodology; Section 3 presents and discusses the classification and depth correlation results; and Section 4 summarizes the conclusions.

2. Methodology

2.1. Materials and equipment

A miniaturized PBF-LB device developed at the Paul Scherrer Institute (PSI) [36] was selected for this study. This setup replicates the commercial PBF-LB process and can be integrated into synchrotron beamlines for simultaneous in-situ X-ray measurements. Its compact size (height: 520 mm, width and depth: 280 mm and 260 mm, respectively) and lightweight (25 kg) design make it easily transportable to synchrotron beamlines. The device features two glassy carbon windows, enabling the X-ray beam to access the powder bed through the rear window, while the transmitted X-ray beam reaches the detector outside the chamber through the front window. Fig. 1 illustrates the main components of the mini-PBF-LB device. The printing chamber includes a 12×12 mm^2 build plate and a hopper-based recoating system equipped with multiple doctor blades. Before each recoat, the build plate is lowered by a distance equal to the layer thickness. Powder is then dispensed by gravity from the hopper, with excess powder removed by the doctor blades. During and before operation, the chamber is flushed with high-purity Argon gas (99.996%) from several inlets, including a small cavity within the recoating system, to ensure the removal of by-products from the laser-material interaction zone. The oxygen level is continuously monitored to maintain its stability below 2000 ppm. A more detailed description of the device is available in [40].

A dual-mode fiber laser (redPOWER, SPI Lasers Ltd, UK) with a maximum power of 500 W, operating at a wavelength of 1070 ± 10 nm and a beam quality factor of $M^2 < 1.1$, was used in this study. Both the laser and the scanning head are controlled via an SP-ICE−3 board and WeldMARK software (Raylase GmbH, Germany). The laser beam is collimated into a parallel Gaussian beam and directed into a 2-axis deflection-scanning unit (SuperScan III, Raylase GmbH, Germany) with an 8 mm input aperture. Two HR-coated fused silica mirror galvanometers facilitate the scanning of the laser beam over the powder bed. The beam is then focused through an F-Theta lens (Sill Optics, Germany) with a 163 mm focal length, producing a focused beam with a spot size of 27.5 µm in diameter at $1/e^2$ and a depth of field of

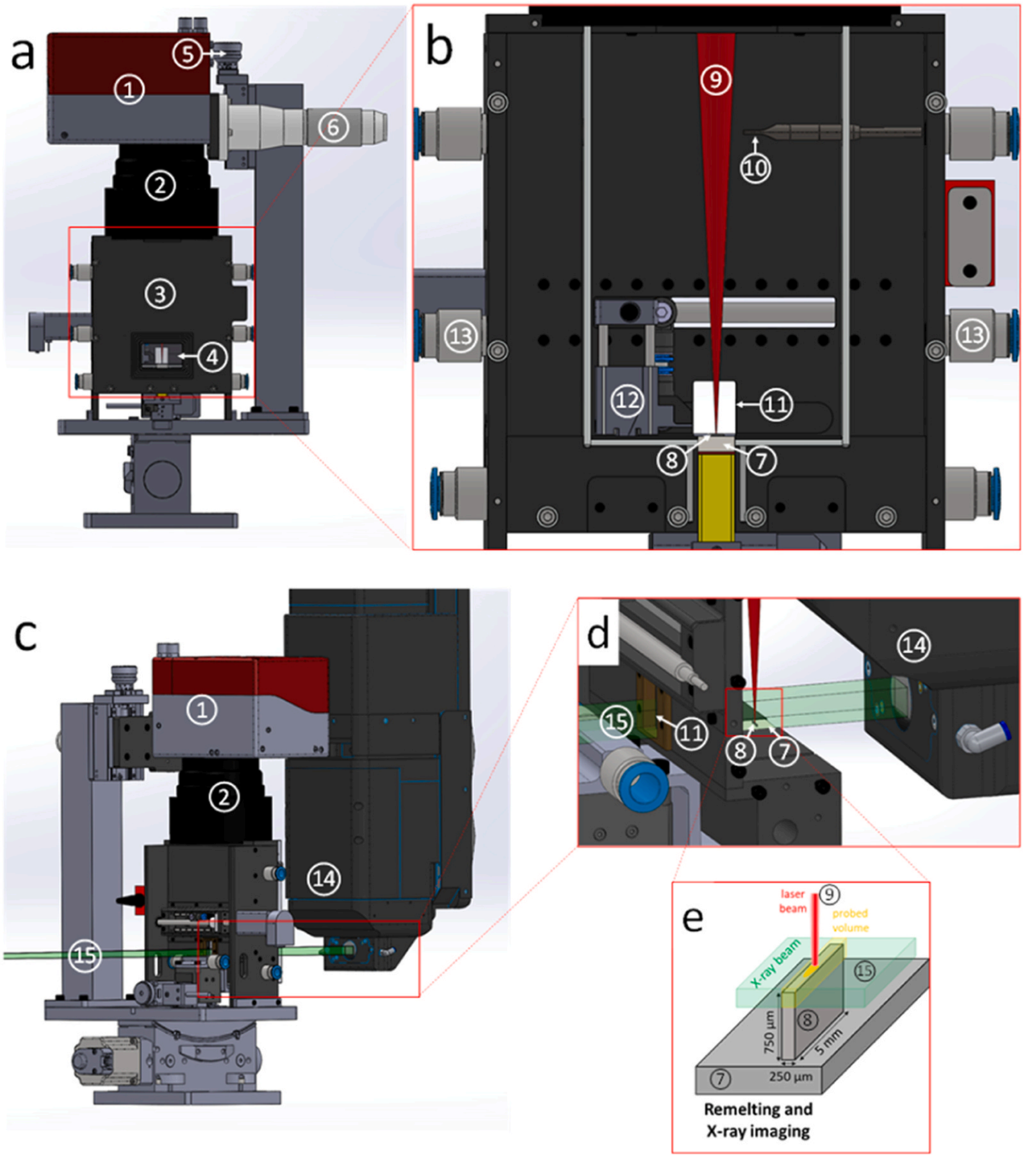

Fig. 1. Front view of the miniaturized PBF-LB device. (a) with and (b) without the front door; schematic view of operando x-ray radiography setup at the synchrotron beamline (c) and its magnification (d); (e) thin wall geometry in presence and absence of powder bed. 1) scanning head, 2) F-theta lens, 3) front door, 4) X-ray exit window, 5) vertical stage to change focal length, 6) laser collimator, 7) build plate, 8) sample, 9) laser beam, 10) AE microphone, 11) X-ray entrance window, 12) powder hopper and re-coater, 13) gas inlet and outlet, 14) microscope, 15) polychromatic X-ray beam.

approximately 1 mm. The laser operated in continuous mode and pulsed mode with pulse repetition rate of 250 kHz and a nominal pulse duration of 2 µs respectively.

A gas-atomized 316 L stainless steel (1.4404) powder (OC Oerlikon Corporation AG, Switzerland) with the chemical composition listed in Table 1 and a particle size distribution in the range of 15–45 µm was selected for this study. The morphology of the powder particles was observed as predominantly spherical, with the presence of occasional satellites. Similarly, a gas-atomized Ti6Al4V ELI (grade 23) powder provided by (AP&C, GE Additive, Canada), with the chemical composition also listed in Table 1 and a particle size distribution ranging from 15 to 53 µm, was selected. The morphology of these particles was also observed as predominantly spherical.

Thin walls were prefabricated using these powders under optimized printing conditions using a Sisma MYSINT100 PBF-LB machine, equipped with a 200 W laser and a focal point beam size of 30 microns. A total of 40 walls of 316 L stainless steel and 10 walls of Ti6Al4V were produced. The resulting printed walls measured approximately 750 µm in height, 300 µm in thickness, and 5 mm in length in their as-built state (Fig. 1). A wall thickness of 300 µm was chosen for two primary reasons. First, it needed to be thin enough to allow adequate X-ray transmission, enabling high-speed X-ray imaging. Second, the effects of top and side

Table 1
Nominal chemical composition of the 316 L stainless steel and Ti6Al4V feedstock powders (wt%).

316 L SS	Element	Fe	Cr	Ni	Mo	Si	C	Other
	wt%	Balance	17	12	2.5	2.3	0.03	≤ 0.5
Ti6Al4V	Element	Ti	Al	V	Fe	O	C	Other
	wt%	Balance	6.3	3.9	0.25	0.13	0.08	≤ 0.02

surface roughness, along with geometrical inaccuracies, become more pronounced with lower wall thicknesses, resulting in non-uniform heat dissipation and projected laser energy distribution during the re-melting process. Geometrically, these walls exhibited slight variations in thickness, with partially attached powder particles evident along both sides. Additionally, laser-induced ripples on the top surface introduced irregularities and roughness. Collectively, these geometric characteristics influence the boundary conditions of the solidified structure. Under certain process conditions, such geometrical variations can trigger instabilities significant enough to surpass the keyhole threshold specific to the material-wall system. To prepare the walls for further processing, the top surface was slightly ground to remove the bulges formed at both ends due to laser acceleration and deceleration. Subsequently, the thin walls were inserted into the mini-LPBF system at the two beamlines for the laser remelting step.

For the experiments, laser scanning of the top surface of the wall was performed with the laser defocused to a diameter at least twice that of the nominal focus (60 μm diameter). This was combined with increased nominal power and substantially reduced scanning speed to achieve the temporal resolution required for capturing regime instabilities and subsequent thermomechanical phenomena (full table outlining experimental parameters in appendix A).

The scan speeds employed in this study (30–100 mm/s) are lower than those used in production LPBF. This is dictated by the operando imaging configuration: at the X-ray frame rates used here, lower scan speeds are required to resolve the melt-pool and keyhole dynamics with sufficient fidelity to correlate them with the acoustic emission. The regime transitions of interest are local phenomena, governed by the energy coupling and vapor dynamics at the laser-material interaction zone rather than by the translation speed of the laser, so the associated acoustic signatures are expected to remain present at higher processing speeds. Validation at production-scale speeds is left to future work.

One or more laser scans were carried out on each wall, where for some scans fresh powder was present on the top of the wall, progressively altering the top surface geometry and introducing variations in track height between successive passes. These modifications gave rise to non-uniform heat dissipation along the wall, driven by the formation of keyhole porosities and other geometric irregularities. Height differences along the wall also affected the laser focus and modified the projected intensity profile on the top surface. In addition, the residual surface waviness from previous remelting passes introduced localized changes in the laser beam incident angle and absorptivity.

The variation in the z-height of the top surface of the walls after laser melting was measured, with a maximum deviation of approximately 160 μm. Assuming the laser interaction occurs around a defocused plane corresponding to twice the focal spot size, a height fluctuation of ±80 μm would lead to an estimated change in the laser spot diameter of approximately 6–7%. This estimate was obtained from Gaussian beam propagation theory, using a beam waist radius of 13.75 μm at 1070 nm and a Rayleigh length of ~0.5 mm.

Regime instability phenomena were deliberately triggered under constant processing parameters by selecting a parameter set near the conduction-to-keyhole transition, guided by state-of-the-art scaling laws [41]. Regime transitions from conduction to stable keyhole, and from stable to unstable keyhole, were observed in both single- and double-line scans without altering the laser parameters. These instabilities persisted from several hundred microseconds to tens of milliseconds. Operando X-ray imaging revealed that such regime instabilities are not isolated to scan initiation or termination regions but may also occur mid-scan, regions traditionally considered to be in steady-state conditions [5].

A membrane-free optical microphone (Eta250 Ultra, XARION Laser Products, Austria) was chosen as an acoustic sensor to capture airborne acoustic emissions from the laser-material interaction zone within the inert atmosphere. This microphone operates on the principles of interferometry, enabling it to detect signals across a frequency range of 10 Hz to 1 MHz. At the heart of the microphone is an optical interferometer, which consists of two semi-transmissive mirrors set at a distance equal to a multiple of the laser half-wavelength. This arrangement creates constructive interference of the transmitted laser beam. As sound waves pass through the microphone's etalon, they cause density changes in the air, which in turn alters the optical refractive index of the medium. This change affects the laser's propagation speed and wavelength through the etalon, disrupting the constructive interference condition between the mirrors. Through interferometry, variations in laser intensity and corresponding pressure levels of the sound waves can be measured. The XARION microphone was installed in the PBF-LB chamber, 100 mm above the powder bed, directly above the processing zone, with its mirrors aligned parallel to the build plate (Fig. 1 showing integration of microphone) to maximize the information gathered from the laser-material interaction zone. To ensure that effects up to 1 MHz could be captured, the signal was sampled with a sampling frequency of 2 MHz. In order to be able to characterize the background noise, the acoustic emission acquisition started before the laser was turned on. This resulted in a measurement of the background noise for every recording.

This all resulted in a dataset consisting of 45 scan lines of two different materials and two different laser modes. The full dataset was manually labelled identifying which frame regime transitions occur. Note that for the quantified evaluation, the beginning and end of every scan line (10 ms) was cut off as the edges exhibited some rounding after remelting which affected the laser incidence angle.

2.2. *Operando X-ray imaging and image processing*

The operando X-ray imaging experiments were conducted at two beamlines: the Tomographic Microscopy and Coherent rAdiology experimenTs (TOMCAT) beamline of the Swiss Light Source (SLS), and the high-speed imaging beamline ID19 at the European Synchrotron Radiation Facility (ESRF). At the TOMCAT beamline, a polychromatic X-ray spectrum, generated by a 2.9 T bending magnet and filtered with 5 mm of Sigradur and 200 μm of Si, was used for the experiments, providing energies ranging from 10 to 55 keV, with the peak of the energy spectrum around 20 keV. The X-rays passed through the 316 L stainless steel walls while the laser impinged perpendicularly onto the top surface of the wall. The propagated X-rays were then converted into visible light using a 150 μm thick LuAG:CE scintillator and recorded with a 4x microscope (Optique Peter, France), coupled to an in-house developed GigaFRoST detector. This detector features a 2016 × 2016 pixels CMOS imaging chip with an 11 μm pixel size and a 12-bit nominal dynamic range. Its readout system enables continuous and sustained data streaming at nearly 8 GB/s to a dedicated high-performance data backend server. Imaging was carried out with a frame rate of 10–15 kHz, a pixel size of 2.75 μm, and an exposure time of 60–95 μs per X-ray image. This performance was achieved by reducing the region of interest to 2016 × 200 pixels, equivalent to a field of view of 5.54 × 0.55 mm^2. The X-ray imaging was triggered by a TTL signal from the laser control card to ensure full synchronization between the start of the laser and X-ray acquisition.

ID19 beamline operated in a polychromatic configuration to achieve a sufficiently high photon flux density for the desired image acquisition rate. The emitted photons from an undulator source (type: u32, gap 11.8 mm) were filtered using diamond (1.8 mm) and aluminum (2.8 mm) attenuators as well as a Beryllium window (0.5 mm). This resulted in a broad polychromatic spectrum ranging between 20 keV and 60 keV with a mean photon energy of approximately 30 keV. High-speed imaging acquisition was performed using an indirect detector comprising a CMOS-based camera (Photron, Japan, type: SA-Z, 1024 × 1024 pixels), lens-coupled to a 250 μm-thick LuAG:Ce single-crystal scintillator with a 5 × (0.14 NA) lens (Mitutoyo, Japan). The effective pixel size was 4 μm, providing a full field of view of 4 × 4 mm^2. The detector was positioned 1.2 m downstream of the sample to utilize propagation-based phase contrast in polychromatic illumination. To achieve a frame rate of 100 kHz (8.39 μs exposure time), the emitted radiation was further collimated by adding 10 compound-refractive lenses (CRLs) approximately 35 m downstream of the source in the X-ray optical beam path. At this frame rate, the SA-Z camera operated with a region of interest of 1024 × 184 pixels, corresponding to a 4 mm × 0.8 mm field of view.

To distinguish between stable and unstable keyhole regimes, identifiable features in the operando X-ray images were relied upon. A stable keyhole was defined by its steady and well-defined morphology, exhibiting minimal fluctuations or structural instabilities. In contrast, an unstable keyhole displayed intermittent collapse and visible porosity formation, evidenced by irregular boundaries, depth fluctuations, and dynamic morphology. The transition from stable to unstable keyhole was marked by the first observable porosity resulting from a keyhole collapse. Conversely, the reestablishment of a stable keyhole regime was defined by both the cessation of porosity generation and the return to a consistent, stable keyhole shape. It is important to note that the time resolution of the X-ray imaging (10 μs to 100 μs per frame) introduces a temporal uncertainty in precisely indexing these regime transitions, potentially affecting the accuracy of their onset or conclusion.

To ensure objectivity and consistency in the regime labeling, the annotation was performed independently by two trained operators following a blinded cross-annotation protocol. Each operator first labeled the full dataset individually, without access to the others' annotations. Subsequently, each operator reviewed and validated the annotations of the other two, again in a blinded manner. Discrepancies between annotators, which occurred predominantly at the temporal boundaries of regime transitions, were resolved through joint review of the corresponding radiograph sequences until consensus was reached. This cross-annotation procedure was adopted to mitigate individual labeling bias and to establish a reliable ground truth for the quantitative evaluation of the proposed acoustic indicators.

Visual inspection revealed that the molten material in the keyhole regime also has a slightly increased gray level compared to the solid material but identifying the melt pool in a single static frame remains challenging. However, with temporal context—viewing the frames consecutively as a video—the edges can be discerned by eye, although automatic detection with image analysis remains out of reach. The pipeline from [2] leverages this fact through a graphical interface for annotation. This pipeline was adapted and released to the community as open-source software in the form of a napari [42] plugin. This plugin allows direct opening of h5 files from the ID19 and TOMCAT beamlines, eliminating the need for prior conversion, and includes an example dataset of reduced size.

The developed pipeline comprises the following steps: laser position extraction, time-windowing, denoising, radial gradient calculation, and annotation.

The first step is the laser position extraction. To extract the laser position, the radiographs are first projected along the y-axis, parallel to the laser beam, resulting in an x-t domain image. The plugin offers three projection modes: 'Default', 'Pre mean', and 'Post median'. The 'Default' projection uses maximum intensity along the y-axis. In 'Pre mean' mode, the mean is computed along the t-axis to estimate the background, dividing each radiograph by the background image before performing the maximum intensity projection along the y-axis. The 'Post median' mode applies a median filter along the x-axis after the maximum intensity projection, removing horizontal stripes in the x-t image. Given the constant laser speed and frame rate, the laser appears as a continuous line in the resulting x-t domain image. This line, representing the laser position over time, can then be annotated using a napari shapes layer within the plugin.

Secondly, to simplify the annotation of the geometric features of the melt pool, the laser is tracked using a sliding window of a specified size. Each radiograph is cropped around the laser position with adjustable left and right margins, which can be set in the plugin. The result is a new image layer where the laser appears static, accompanied by a shape layer containing a vertical line that indicates the laser position in the new image layer.

Next, to highlight the static melt pool against the moving background and reduce noise, the plugin includes an option to apply a median filter. The footprint size of the filter can be adjusted along all three axes (t, x, y).

Following this, the geometry of the melt pool, as seen in the radiographs, is defined by its edges. To visually accentuate the edges, a directed gradient can be calculated. The direction should be perpendicular to the edges for the strongest response. Since the melt pool shape is approximately semi-circular, the gradient is calculated radially from a center that can be moved using the plugin's user interface.

In the final step, the plugin allows tracking points of interest by recording the position of the cursor. These points of interest could be the interface between the melt pool and the un-melted material at the front and rear of the laser's path. Each time the frame is changed (either playing the film or manually scrolling through frames), the current cursor position is saved as the position of the point of interest for the preceding frame. Due to the time-windowing, the melt pool is fixed in place, so any movement of the points of interest is due to changes in the melt pool geometry. The melt pool's geometry changes relatively slowly from one frame to another, making it possible to follow points with the cursor as the frames are played back.

2.3. Physics-based acoustic signal processing indicators

While it has been shown that acoustic emissions are linked to the formation of (unstable) keyholes, very little work exists aiming to model the exact mechanism. Sun et al. [35] model the keyhole using whistle aeroacoustics, where the shape influences the frequency of the emitted whistle and the vapor outflow provides the gas flow. However, the speed of the fluctuations of the keyhole (from 2.5 kHz up to 50 kHz [8,43]), the time-frequency uncertainty principle, and the fact that the measured recordings show multi-tonal or wideband signals, make it a challenge to use this model for practical regime classification. Therefore, in this work a novel model based on amplitude modulation effects is proposed.

The phenomenological model assumes the acoustic signal originates primarily at the liquid-gas interface via metallic vapor generation [26,44]. Based on this assumption, a novel phenomenological model is constructed where the vapor plume flowing out of the keyhole is assumed to generate an acoustic signal present in a wide frequency band without specifying the frequency with the highest energy concentration [35]. In this phenomenological model, the main difference between the conduction regime and the keyhole regime will be the amount of vapor outflow. In the case of a continuous laser, this practically results in a higher amplitude of this wideband acoustic signal but without any sudden changes in amplitude [45]. When the keyhole changes to an unstable keyhole, the keyhole collapses and thus the vapor gas outflow is expected to change suddenly [26]. In case of a pulsed laser, one can expect an additional amplitude modulation effect, where the pulse frequency of the laser also modulates the vapor outflow.

As this phenomenological model depends on amplitude changes of the acoustic signal through time, the signal processing steps will heavily rely on the theory of amplitude modulation in order to detect the different regimes [46]. One advantage of this model is that any frequency band can be selected for the monitoring of the amplitude changes. This allows for more design freedom, as now frequency bands can be selected with as little as possible noise. As it is observed that in lower frequency ranges there is significantly more background noise, this work focusses on higher frequency ranges in comparison to previous work, which often attempts to monitor the keyholes at the fluctuation frequencies of the keyhole [34,47]. All the indicators are based on three steps: a denoising step using spectral subtraction, a filtering and demodulation step, and a final step where the energy of the resulting envelope/signal is computed.

A noise removal step can greatly increase the signal quality [48] as the recorded acoustic signal is distorted both by interfering acoustic signals, such as those related to the flow of shielding gas, and electromagnetic interference. The noise removal by spectral subtraction uses an estimate of the noise power spectrum, which is then subtracted from the measured signal in the time-frequency domain [49]. The power spectrum density (PSD) of the noise is estimated using the welch estimate [50] of the acoustic data captured before the laser is turned on. Looking at the PSD of the noise in Fig. 2, two noise components can be identified: a low frequency noise (sub 100 kHz) and discrete peaks in the higher frequencies. As the second noise component consists of periodic, discrete peaks, it is assumed that these peaks are due to electro-magnetic interference.

Because the acoustic acquisition was started before the laser to characterize the background noise, the acoustic data was synchronized with the video by detecting the arrival of the signal from the melt pool. The time of arrival of the acoustic signal was determined based on the energy in the signal after denoising within a 0.2 ms window exceeding that of the background noise. Through this approach the time of arrival did not need to be taken into account. Throughout the scan, the travel time from melt pool to microphone varied less than 0.1 microsecond along the scan because the source displacement was small relative to the source-to-sensor distance. Therefore, the change in travel time was neglected.

The result of denoising is shown in Fig. 3, which visualizes the Short-Time Fourier transform (STFT) of a scan track before and after denoising. The proposed denoising procedure is able to denoise the discrete high frequency peaks. While the energy of the low-frequency noise is reduced, there remains significant energy in these noisy frequency bands.

The second step is a filtering and demodulation step, which will be designed based on the different discussed phenomenological models of the acoustic emissions when employing a pulsed or a continuous laser. The exact filtering and demodulation techniques will be discussed later in the sections describing the different indicators. All used filters in this work are Butterworth filters [51] applied using a forward backward filter to achieve a zero-phase offset [52]. The chosen cutoff frequencies were based on the minimization of the confusion between the different regimes with a full sensitivity analysis in Appendix B.

Hilbert based demodulation and quadrature demodulation techniques are both considered. The Hilbert based demodulation extracts an envelope, which describes the instantaneous amplitude of a signal, by computing the magnitude of the analytical signal. The analytical signal of x(t) is defined through its Fourier transform:

$$X_a(f) = X(f) + \mathrm{sgn}(f)X(f)$$

where X(f) is the Fourier transform of x(t) and sgn(f) is the sign function.

Hilbert based demodulation is effective in extracting the envelope of

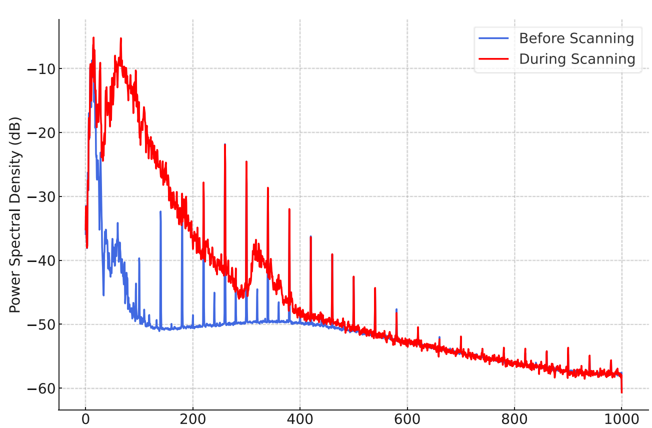

Fig. 2. The PSD of the measured signal and the background noise before the laser is turned on.

vibration signals in which the frequency distribution of the carrier is also unknown [53]. Consequently, it will be used when demodulating the wideband signal from the vapor gas outflow for which the central frequency is unknown. The demodulation of the wideband signal is performed in an effort to extract the amount of gas being formed at every timepoint.

When the exact frequency of the carrier is known, quadrature demodulation is used [46]. This technique extracts the envelope describing the instantaneous amplitude by decomposing the signal in an I (in-phase) channel and a Q (quadrature-phase) channel. Formally, the envelope of a signal x(t) can then be computed as:

$$e_x(t) = 2\sqrt{I(t)^2 + Q(t)^2}$$

.

The main benefit of this demodulation technique is that it only demodulates one specific carrier frequency, chosen up front. It is therefore useful when working with a pulsed laser.

The final step is based on the energy of the output of the filtering and demodulation step, where the resulting signal is squared and averaged over a 2500-point sliding window resulting in a time resolution of 1.25 ms [2]. To determine the threshold used for classification on this final energy value, both for the keyhole detection and the unstable keyhole detection, a leave-one-out cross validation scheme is used per scan line where the threshold is optimized with respect to the F1 score on the validation data. This makes sure that the predictions on a certain scan line are not based on labelled data from that specific scan track. The only exception to this validation scheme concerns the Ti6Al4V case with pulsed laser, as in this case only a single scan track is available exhibiting keyholes.

2.3.1. *Filtered energy baseline (FEB)*

The baseline indicator against which the other indicators will be compared is the Filtered Energy Baseline (FEB) where the idea is to measure the total amplitude of the gas outflow out of the melt-pool. Therefore, the measured acoustic signal is only filtered, and two thresholds are considered on the same output, one to determine the occurrence of a keyhole and one to determine when a keyhole transitions from stable to unstable.

For the continuous laser case, the filtering consisted of a high-pass filter. This is due to the observation that the keyhole regime had energy content in a wide frequency band in addition to the lower frequencies containing a lot of noise [23]. Note that the chosen high-pass filters (cutoff frequency of 150 kHz for 316 L and 210 kHz for Ti6Al4V) have a significantly higher frequency range than previously indicated keyhole fluctuation frequencies (2.5–50 kHz). However, these latter frequencies lie within a frequency band considerably corrupted by noise, and the conduction regime also contains a significant amount of energy in these lower frequency bands. This all resulted in worse performance when including these lower frequencies. The cutoff frequencies were different between Ti6Al4V and 316 L due to the significant difference in conduction regime acoustic emissions of Ti6Al4V and 316 L. This difference is likely due to differences in vaporization of the two materials.

For the pulsed laser case, it was observed that the pulse frequency of the laser distorted the higher frequencies, resulting in a poor performance of a high-pass filtered signal, which is why in this case the FEB method included a low-pass filter instead of a high-pass filter at 230 kHz as the pulse frequency of the laser was 250 kHz.

2.3.2. *Continuous laser: envelope energy method (EEM)*

In addition to the FEB, the amplitude modulation based phenomenological model can be applied to the high-passed signal. The occurrence of the keyhole and unstable keyholes can then be detected by monitoring the energy of the low and high frequency content of the envelope. Elevated energy in the low frequency content of the envelope indicates a high amplitude in the acoustic signals, and thus the

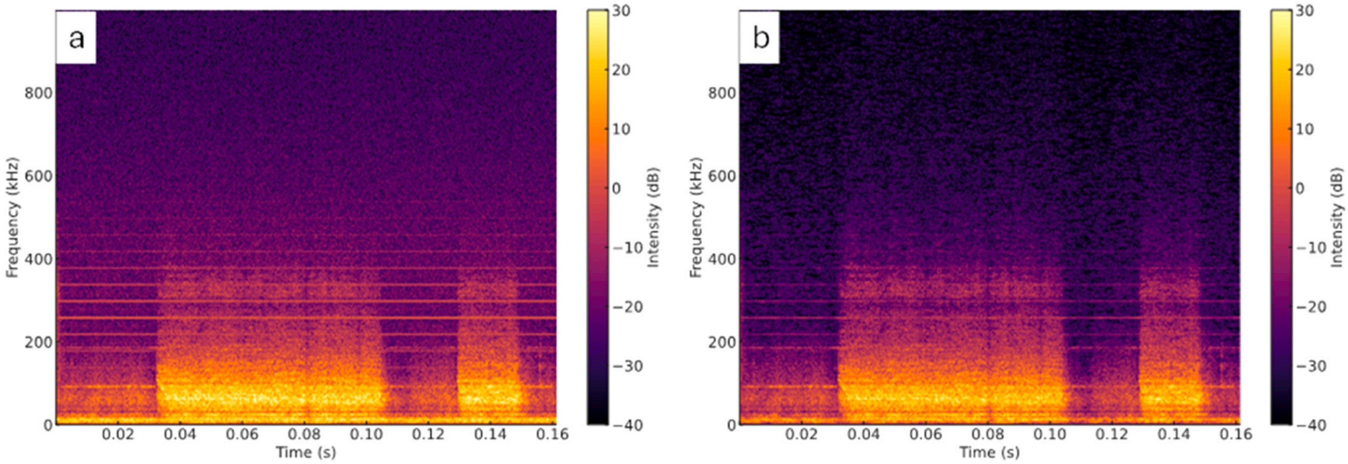

Fig. 3. The short-time Fourier transform of experiment SS-C-M17 (a) before denoising and (b) after denoising.

occurrence of a keyhole causing a large amount of gas outflow. High energy in the high frequency range then indicates that the gas outflow of the keyhole changes abruptly, i.e. the occurrence of an unstable keyhole. The full procedure is shown schematically in Fig. 4.

For the filter cutoff frequencies, the same cutoff frequencies for the initial high pass filter are used as the FEB. The low pass filter on the envelope is set at 40 kHz for SS316L and 80 kHz for Ti6Al4V. The high pass filters on the envelope are set at 40 kHz for SS316L and 80 kHz for Ti6Al4V. Note that the utilized cutoff frequencies are different for the two considered materials, as the melt pool dynamics such as the intrinsic oscillations present in stable keyholes are also different between these materials [45,54,55].

2.3.3. Pulsed laser: double demodulation energy method (DDEM)

Following the phenomenological model, it is expected that in the pulsed laser case the amplitude of the wideband signal generated by the gas outflow will be modulated by the laser pulses, as the vapor gas will only be formed when the laser is emitting. To validate this assumption, a pulsed laser signal is demodulated and the STFT plot is shown in Fig. 5. A clear energy concentration is noticed in the envelope at the laser pulse frequency of 250 kHz when the keyhole is open. One can then expect that in the case of a stable keyhole, the pulse laser modulation of the wideband signal generated by the vapor gas is consistent as long as the keyhole remains open. However, the pulsed laser modulation is not purely concentrated at the 250 kHz frequency. This is caused by the collapsing of the unstable keyholes, thereby interfering with the laser beam path and reducing the generation of vapor gas.

Considering these relations, the signal processing pipeline consists of two filtering and demodulation steps. First, a band-stop filter is applied to the pulsed laser frequency and its harmonics, with a stopband width of 4 kHz, as there was no relation between the amplitude of the 250 kHz frequency in the raw signal and the regimes seen in the in-situ synchrotron measurements. Then the signal is demodulated for the first time using a Hilbert transform. The result of this first demodulation is

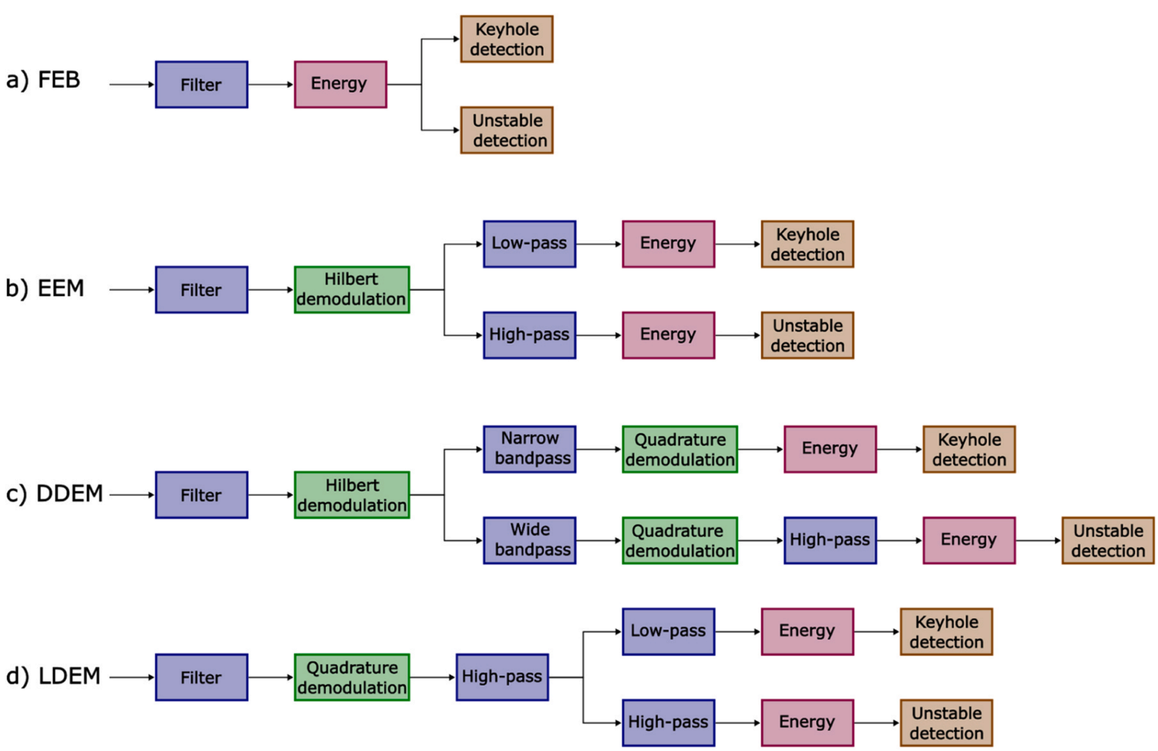

Fig. 4. Flowchart depicting schematically the a) FEB b) EEM c) DDEM d) LDEM.

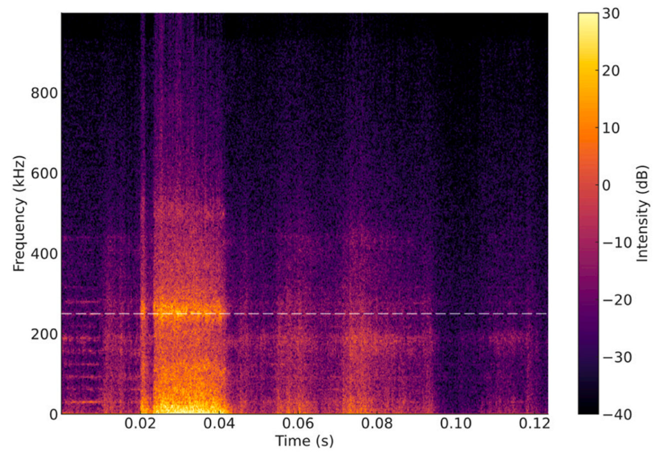

Fig. 5. The short-time Fourier transform of the demodulated signal of experiment SS-P-RM2. A keyhole was formed from 0.02 s until 0.021 s and from 0.0234 s to 0.0412 s of which the period from 0.0249 s to 0.0383 s was unstable. The horizontal dashed line outlines the 250 kHz frequency. Note that after demodulating there is still a clear concentration at 250 kHz when a keyhole is present.

shown in Fig. 5, where one can see that there is still a clear concentration around the 250 kHz frequency band as mentioned previously. Therefore, it can be assumed that the vapor outflow is modulated by the pulsed laser, and a second demodulation step will then be performed in order to obtain the melt pool fluctuations.

The obtained envelope is then filtered using a bandpass filter around the pulse laser frequency. In this step, two different band pass filters around the pulse laser frequency are used for the keyhole detection and the unstable keyhole detection. For keyhole detection, the pulse laser frequency is demodulated using quadrature demodulation after a narrow band-pass filter in order to extract the slow changes of the pulsed laser modulation. The frequency bands were set at 225–275 kHz for SS316L and 30–570 kHz for Ti6Al4V.

For unstable keyhole detection, a wider band-pass filter (20–480 kHz for both materials) is chosen followed by a high pass filter (SS316L: 30 kHz, Ti6Al4V: 140 kHz) on the final envelope, in an effort to identify sudden changes in the pulsed laser modulation. These sudden changes in pulse laser modulation are then indicative of an unstable keyhole. The full pipeline of the DDEM indicator is shown schematically in Fig. 4.

2.3.4. *Pulsed laser: laser demodulation energy method (LDEM)*

An alternative assumption for the pulsed laser case is that the pulsed laser creates a direct pressure wave at the pulse laser frequency. Therefore, a final indicator is proposed where the denoised signal is band-passed around the pulse laser frequency (20–480 kHz) and the envelope is computed. However, as already mentioned, the very low frequency energy changes (SS316L: 5 kHz, Ti6Al4V: 7.5 kHz) of the pulsed laser frequency are not correlated with the synchrotron measurements and are therefore filtered out. The remaining envelope is then once again subjected to a low-pass filter for the keyhole detection (SS316L: 30 kHz, Ti6Al4V: 150 kHz) and a high-pass filter for the unstable keyhole detection (SS316L: 10 kHz, Ti6Al4V: 230 kHz). The full procedure for the LDEM is depicted schematically in Fig. 4.

3. Results and discussion

In Fig. 6, the results for a SS316L scan track with powder are shown. The melting initiates in conduction mode and, at approximately 32.0 ms, transitions into a stable keyhole regime, followed by the onset of instability. As the keyhole cavity deepens, the enhanced absorption of laser energy, driven by internal multiple reflections, leads to rapid melt pool expansion. This 'drilling' action peaks in depth at 40 ms. At this stage, elevated temperatures at the base of the keyhole create a steep thermal gradient relative to the melt pool perimeter, triggering strong

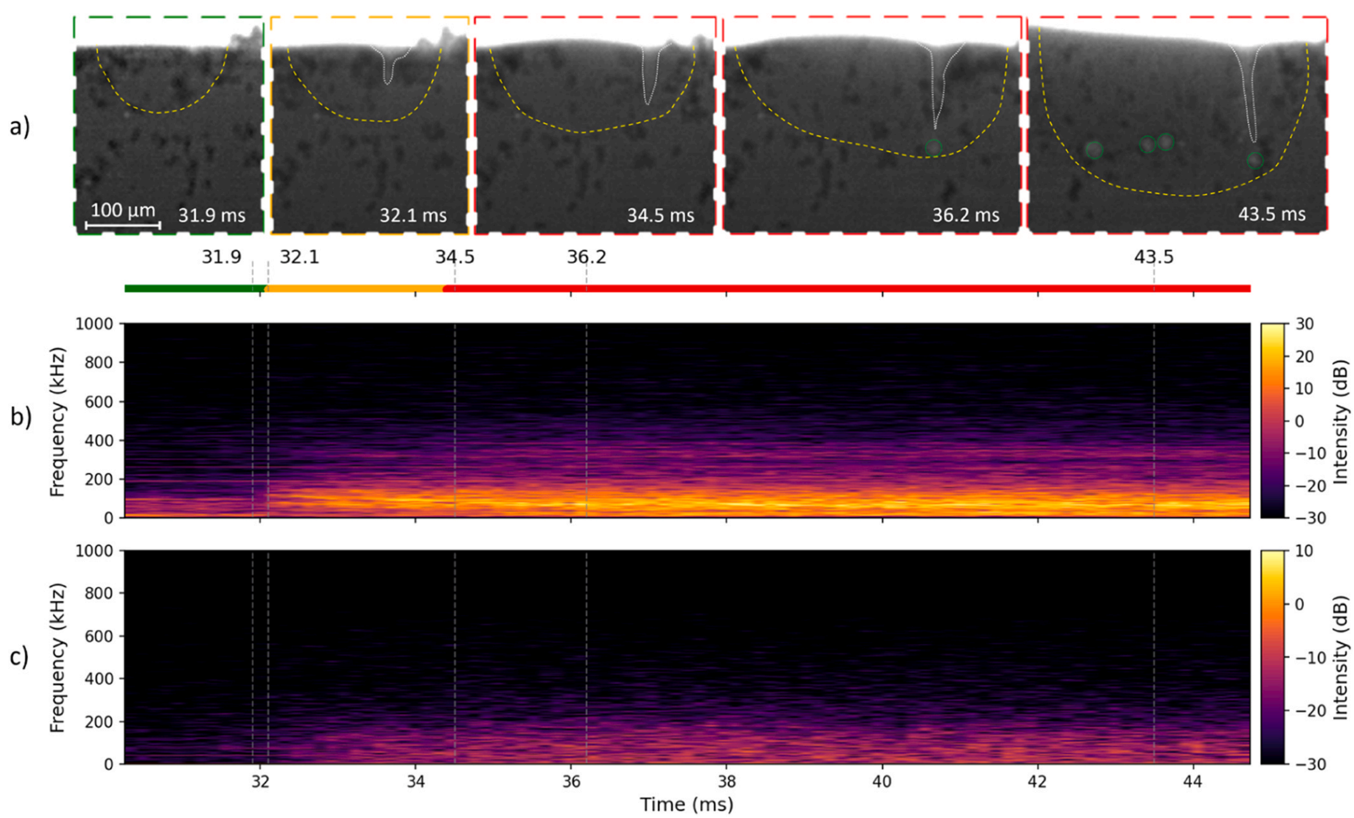

Fig. 6. Short section out of a SS316L scan line with continuous laser (SS-C-M17). a) Synchrotron images b) STFT of the signal c) STFT of the demodulated signal.

Marangoni convection that redistributes heat within the molten region [11].

Looking at the acoustic data, it can be seen in the STFT of the measured signal after denoising (Fig. 6b) that when the keyhole opens, additional high frequency components arise. When these high frequency components are demodulated (Fig. 6c), one can observe that when the keyhole is open, the fluctuations present in the acoustic signal progressively contain higher and higher frequencies until the keyhole transitions to an unstable state. Thus, showing that, sudden fluctuations of the acoustic energy are indeed indicative of keyhole instabilities.

In order to understand the effectiveness of the proposed indicators, they are visualized in Fig. 7 for the full scan track, accompanied by the extracted depression depth, melt pool width and depth. Throughout the full unstable keyhole regime (34.5–103 ms), intermittent transitions between unstable and stable states are observed. These fluctuations are associated with changes in the morphology of the keyhole walls, as shown in Fig. 7, which alter the pattern of internal reflections and reduce absorbed laser energy. Reduction in energy input diminishes both evaporation rates and the recoil pressure sustaining the keyhole cavity. Consequently, the keyhole depth decreases, promoting a return toward a more stable regime. The trend of decreasing keyhole depth continues until the cavity closes entirely, marking a transition back to conduction mode at 104.5 ms. However, due to the complex and varying boundary conditions, stemming from local changes in wall thickness, semi-attached metallic particles, and variations in laser incident angle caused by surface roughness, subsequent transitions from conduction back to stable and unstable keyhole regimes are observed. These evolving conditions highlight the dynamic and sensitive nature of regime stability in the PBF-LB/M process. Despite the stochastic nature of the process, both keyhole indicator, which aims to capture the overall level of vapor outflow by computing the energy of the low frequency content of the envelope, and the instability indicator, which aims to

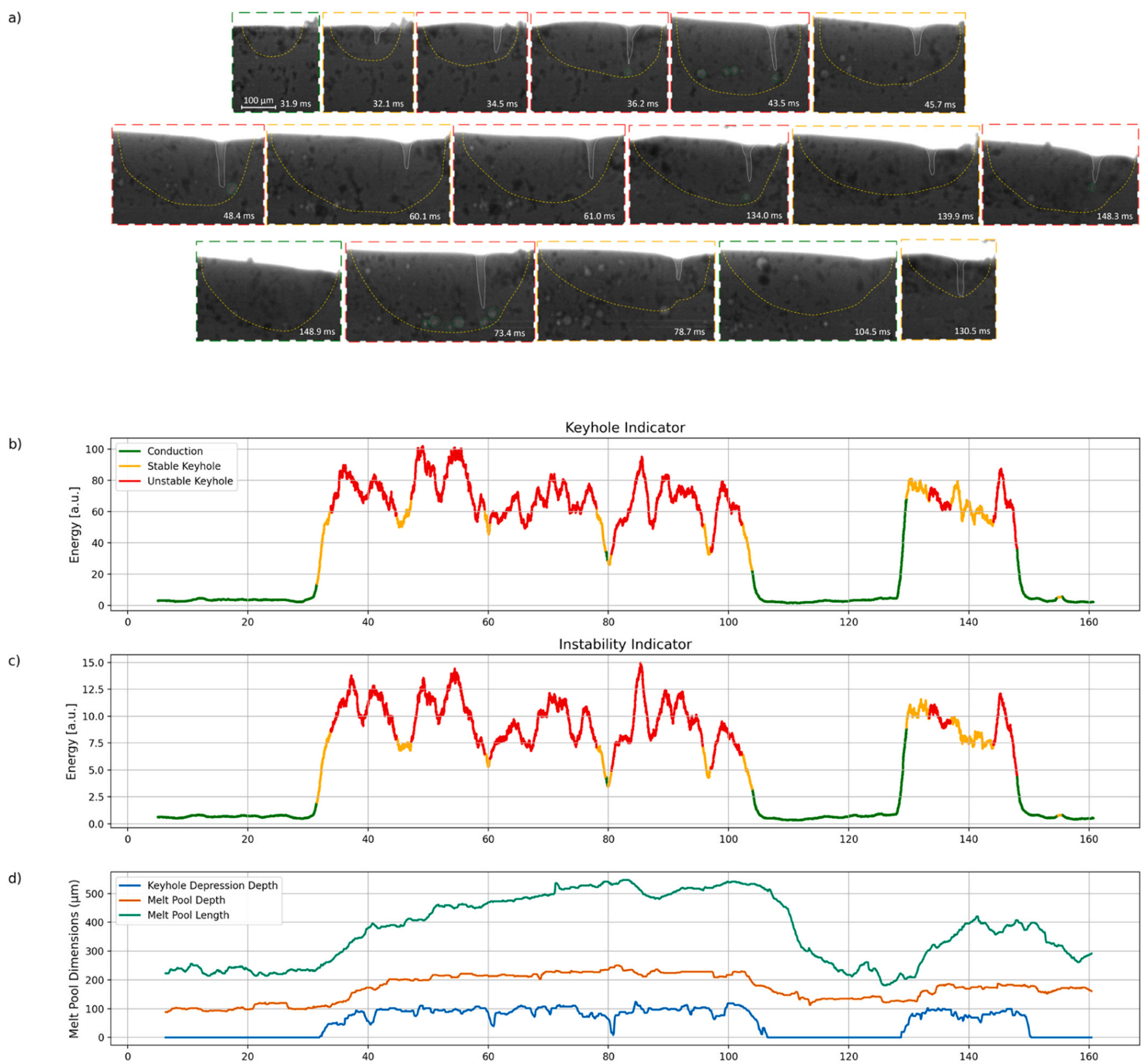

Fig. 7. Full SS316L scan line with continuous laser (SS-C-M17).a) Synchrotron images showing stochastic regime transitions b) EEM keyhole indicator c) EEM instability indicator d) Depression depth, melt pool depth, and melt pool length.

capture the sudden changes of vapor outflow by computing the energy of the high frequency content of the envelope, show a good correlation with the regime transitions.

In addition to the investigation into different materials, different laser modes were also investigated. Therefore, Fig. 8 shows a segment of an experiment using a pulsed laser operating at 250 kHz remelting a bare Ti6Al4V wall. The laser scanning starts with a conduction regime which lasts about 33.2 ms followed by direct transition into unstable keyhole, where keyhole collapse generates porosity at the bottom of the melt pool. The acoustic signal behaves notably different in the pulsed laser case, as first of all one can see a clear increase in intensity at the pulse frequency in the STFT (Fig. 8b). In addition, one can observe a wideband effect over a whole range of frequencies when the keyhole opens. As mentioned, the intensity at the pulse frequency (and its harmonics) was not related to any observable effect in the synchrotron videos and was therefore filtered out. The signal after demodulation once again also shows significant energy concentration around the pulse laser frequency when the keyhole is open. In addition, one can also observe the energy spreading over a frequency band in the demodulated signal (up to 500 kHz) when the keyhole is unstable, but a significantly lower spread is visible when the keyhole transitions to the stable regime.

Similarly to the SS316L case, in this scan line several regime transitions also take place between conduction and stable and unstable keyhole (Fig. 9), marking the inter-regime instabilities in a diverse processing condition for a different alloy and different laser. But nevertheless, the proposed acoustic processing pipeline is able to track these changes. Note the correlation between the keyhole regime indicator and the keyhole stability indicator. The high correlation is likely due to the keyhole indicator being related to the vapor outflow, which can be linked to the keyhole depth, and deeper keyholes in turn being more unstable.

In order to validate the indicators for different materials, a comprehensive dataset is gathered across both materials, and the classification performance is shown in Table 2 (confusion matrices are given in Appendix C). The performance for the classification between conduction and keyhole mode using a binary F1-score. The ternary classification task between conduction, stable keyhole and unstable keyhole is evaluated using the weighted average F1 score. Finally, the classification between unstable and stable keyholes is indicated by keyhole stability F1.

Firstly, one can observe a strong correlation between the keyhole indicator and the instability correlation for the continuous laser in Fig. 6. One way to verify the effectiveness of the proposed instability indicator, is through the comparison of the EEM indicator to the FEB. Note that the FEB is very similar to the EEM keyhole indicator, as the former monitors the acoustic energy inside a window while the latter monitors the slow changes instantaneous amplitude of the acoustic signal. This results in a very similar performance on the binary classification task between keyhole and conduction regime as shown in Table 2. But, for the classification between the stable and unstable keyhole regime, the approach of the EEM differs significantly, where the FEB simply sets a different threshold on the same indicator. This results in a difference between the FEB and the EEM indicator on the stable versus unstable classification, where the EEM exhibits a decrease of misclassifications of 6% for the SS316L dataset and 33% on the Ti6Al4V dataset. Thus, showing the benefit of using the sudden changes in acoustic amplitude in comparison to only monitoring the total acoustic energy. Note that due to the relatively low amount of stable keyhole sections in the full dataset, this has a minimal impact on the ternary classification metric.

Secondly, note that the proposed indicators achieve a higher performance on the dataset when employing a pulse laser. This is likely due to the additional amplitude modulation allowing for better separation between the acoustic energy coming from the vaporization and the background noise. Once again, the performance increase is most notable when trying to distinguish between stable and unstable keyholes. For example, for the 316 L dataset, the use of the DDEM methodology

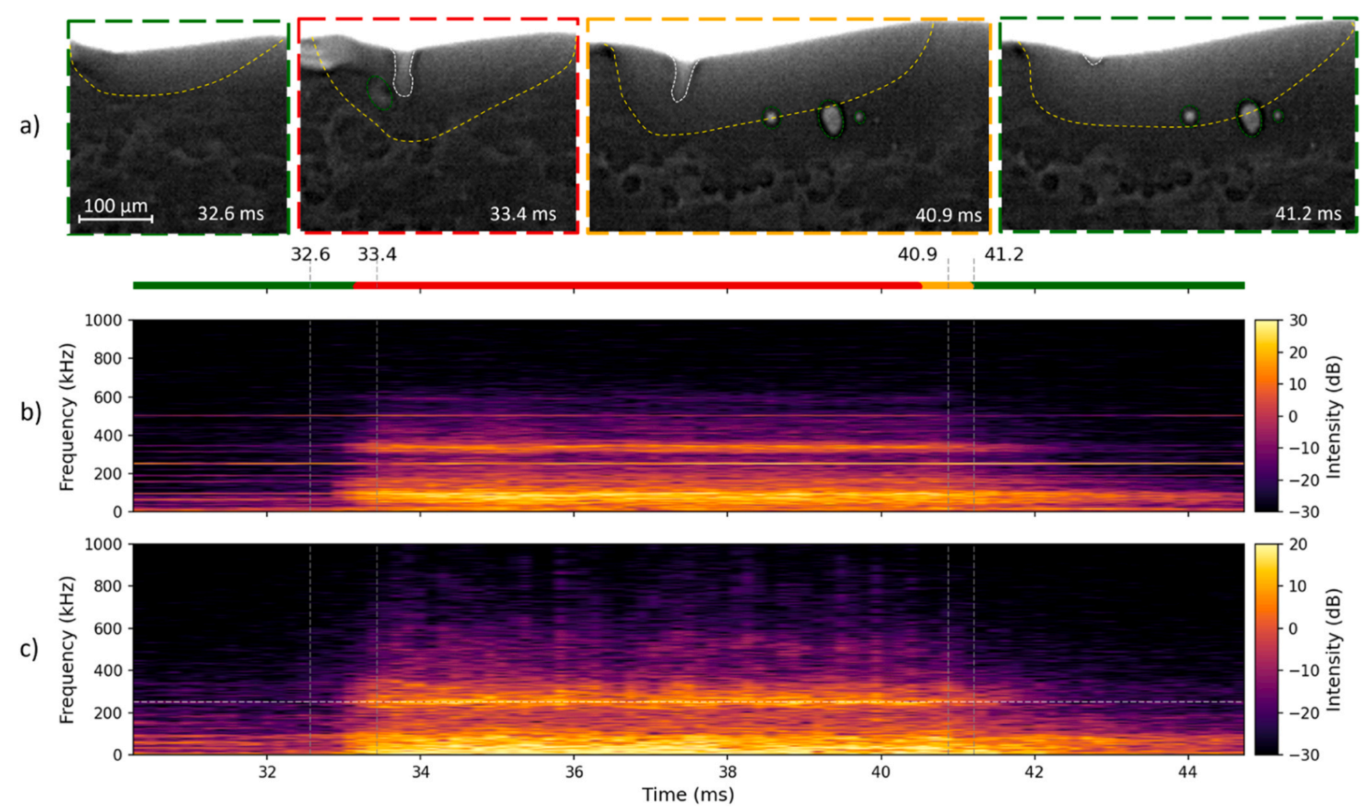

Fig. 8. Short section out of a Ti6Al4V scan line with pulsed laser (Ti-P-RM1). a) Synchrotron images b) STFT of the signal c) STFT of the demodulated signal with a dashed white line indication the pulse laser frequency.

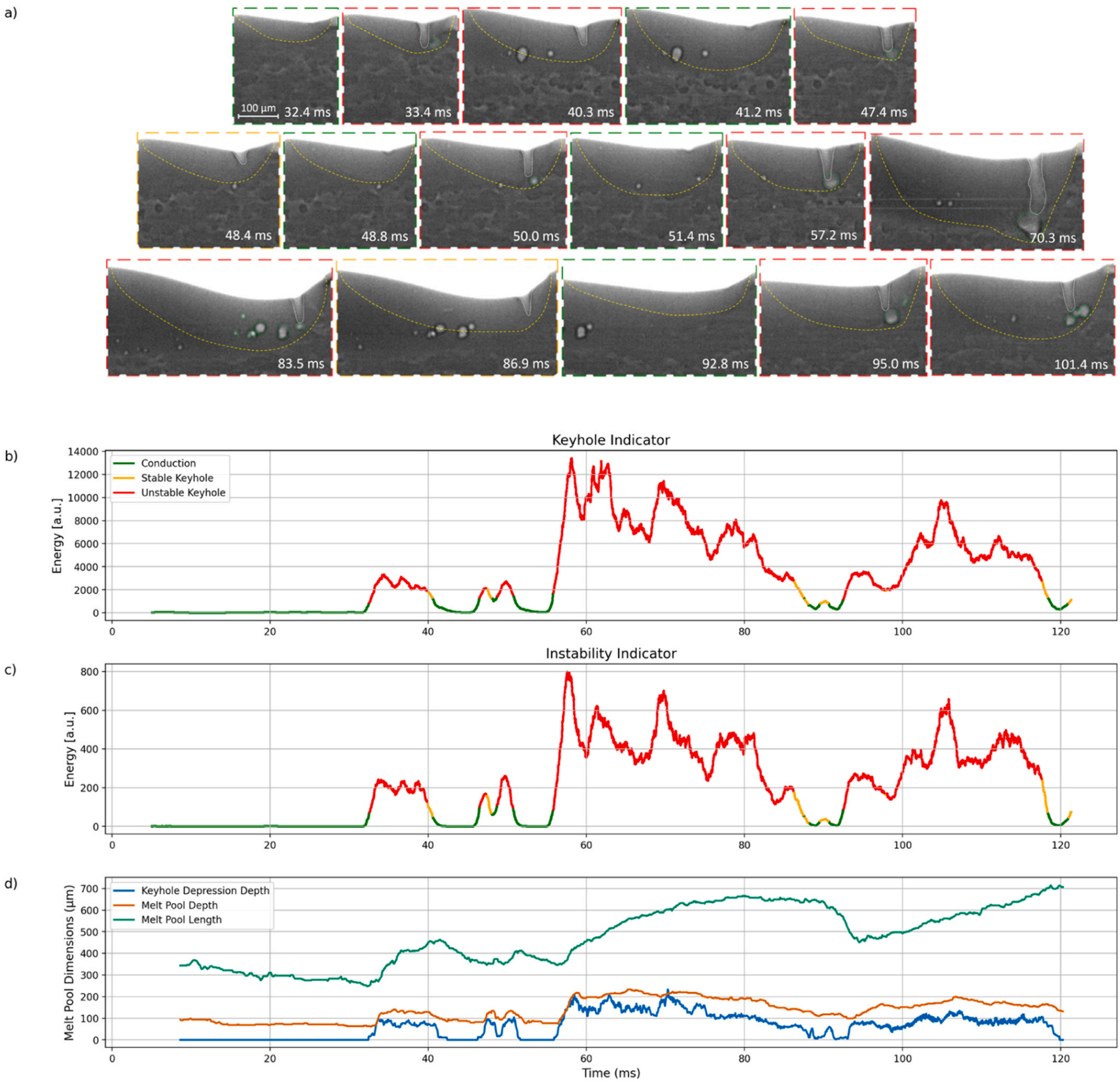

Fig. 9. Full Ti6Al4V scan line with pulsed laser (Ti-P-RM1).a) Synchrotron images showing stochastic regime transitions b) DDEM keyhole indicator c) DDEM instability indicator d) Depression depth, melt pool depth, and melt pool length.

Table 2
Performance of the proposed melting regime prediction indicators across all the considered scan tracks for 316 L steel and Ti6Al4V, considering both continuous and pulsed laser modes. Performance reported in binary F1-score which captures the classification between conduction mode and keyhole mode. The classification between unstable and stable keyholes indicated by Keyhole stability F1. The ternary classification task is evaluated using the weighted average F1 score. As there was only a single scan track of Ti6Al4V with pulsed laser exhibiting keyholes, these results were obtained without cross validated threshold setting and are indicated in cursive.

		316 L			**Ti6Al4V**		
		Conduction-keyhole F1	**Keyhole stability F1**	**Ternary weighted F1**	**Conduction-keyhole F1**	**Keyhole stability F1**	**Ternary weighted F1**
Pulsed	**FEB**	96.08	77.72	92.95	*99.16*	*46.17*	*96.52*
	DDEM	97.59	90.42	96.43	*99.27*	*70.92*	*97.68*
	LDEM	97.08	79.68	93.86	*99.39*	*73.18*	*98.09*
Continuous	**FEB**	94.47	78.44	89.54	99.17	76.28	96.74
	EEM	94.31	80.19	89.76	99.08	83.21	97.25

reduces the number of misclassified points between unstable and stable keyhole by 55% in comparison to the FEB as can be seen in the confusion matrices in Appendix C.

As the proposed model is based on the assumption that the amplitude of the acoustic emissions is related to the amount of vapor gas being generated, and the depression depth of the melt pool being related to the recoil pressure generated by the vapor gas, the indicators can also be adapted for the use of melt pool depth estimation. In the continuous laser case, the depth indicator is the energy of the demodulation of the high pass filtered signal (using the same high pass filter as in the keyhole detection case). For the pulsed laser DDEM case, the energy used is that of the final envelope after filtering, Hilbert demodulation, filtering using the 20–480 kHz filter and pulse laser quadrature demodulation. Similarly, for the LDEM, the energy of the envelope obtained by demodulating the pulse laser carrier is used as the depth indicator. This results in a very similar pipeline with the removal of some of the final filters, as now the intention is no longer to capture the high or low frequency oscillations but all of them.

The relationship between keyhole depth and the corresponding acoustic indicators for Ti-C-RM2 and Ti-P-RM1 are illustrated in Fig. 10 and the Pearson correlation coefficient (PCC) for all the scan tracks where melt pool tracking was performed are given in Table 3. All indicators, on both materials, show a significant correlation, with a p-value lower than 1%. The mean square error performance of a linear indicator of depth is given in Appendix D. There is no difference between the EEM and FEB methodologies, consistent with the previous comment on EEM being better at tracking the sudden changes in depth due to the keyhole collapses, but with no benefit when tracking the slower changes in vapor generation. Due to the imaging speed these sudden changes in depth were difficult to observe in the X-Ray based ground truth and are thus not captured.

When a pulsed laser is employed, the relationship between the acoustic indicators and depression depth becomes notably more linear and exhibits a lower standard deviation, confirming the advantage of pulsed condition for accurate melt pool monitoring. This observation was consistently held across all experiments performed under both pulsed and continuous laser modes, with the pulsed laser condition systematically yielding higher classification accuracy. The observed linearity also highlights the strong coupling between acoustic emissions and keyhole cavity depth, revealing the fundamental dependence of the generated acoustic waves on the metallic jet dynamics that govern recoil pressure and, consequently, the evolution of the keyhole cavity.

Table 3
Pearson correlation coefficient between indicator values and the depression depth of the melt pool.

		FEB	DDEM	LDEM
Pulsed	**SS-P-RM14**	0.869	0.929	0.894
	Ti-P-RM1	0.927	0.941	0.927
		FEB	**EEM**	
Continuous	**SS-C-M17**	0.927	0.927	
	Ti-C-RM2	0.927	0.927	

4. Conclusion

This work introduces a physics-based signal processing framework for acoustic emission monitoring of the PBF-LB/M process, departing from the predominantly machine-learning-driven approaches reported to date. The central contribution is an amplitude modulation model that links airborne acoustic signatures directly to vapor outflow dynamics at the melt pool surface, enabling physically interpretable detection of conduction-to-keyhole transitions and keyhole instabilities without reliance on trained classifiers.

Different envelope-based indicators were developed and validated against operando synchrotron X-ray imaging at two beamlines (SLS and ESRF) across 45 scan tracks in 316 L stainless steel and Ti6Al4V. The EEM indicator, which exploits the frequency content of the acoustic envelope, reduces misclassifications between stable and unstable keyhole regimes by up to 6% and 33% compared to the energy-only baseline on 316 L and Ti6Al4V respectively. More significantly, the use of a pulsed laser introduces an additional amplitude modulation mechanism at the pulse repetition frequency, which the DDEM indicator exploits to achieve a 55% reduction in stable-unstable misclassifications for 316 L. Beyond regime classification, all indicators show a statistically significant correlation with melt pool depression depth, with the pulsed laser condition yielding a notably more linear relationship.

Several limitations should be acknowledged. Firstly, for the T6Al4V pulsed laser case only a single scan track exhibiting keyholes was available, which limits the significance of the results on this case. A further limitation is that the proposed model attributes the acoustic emission to vapor outflow, a quantity that is not measured directly in the present setup. The interpretation is supported indirectly by the wide-band character of the signal, by the correlation between the acoustic indicators and the measured depression depth but direct measurement of vapor velocity or mass flux is left to future work. In addition, the experiments were conducted on a miniaturized PBF-LB/M system on prefabricated thin walls, which differ from production-scale builds in

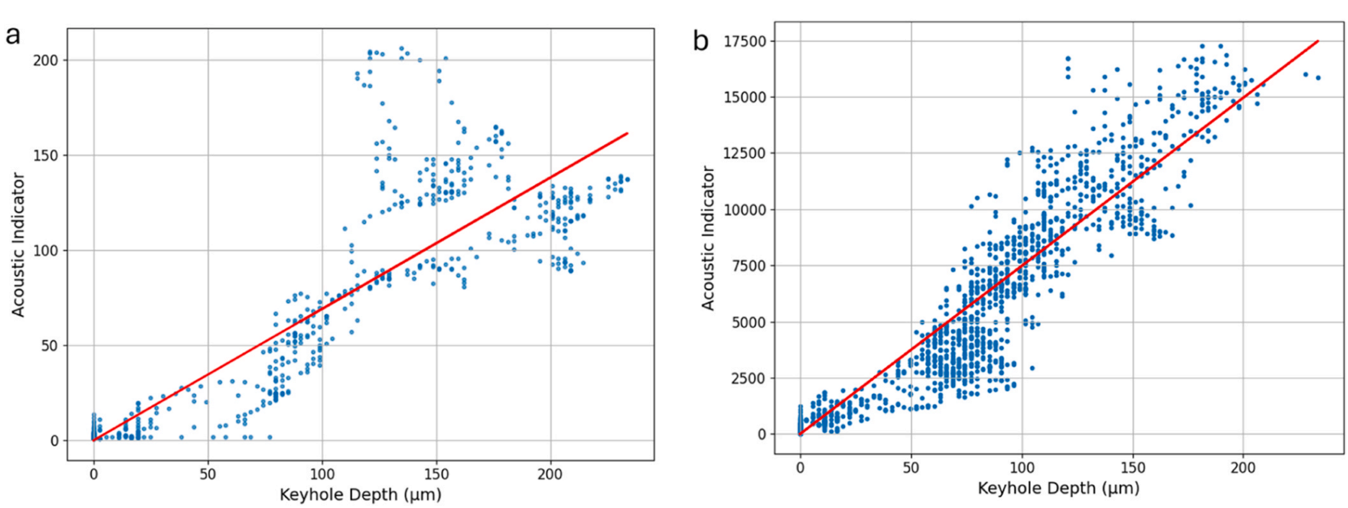

Fig. 10. Keyhole depth correlation with the acoustic indicator and the line of best fit. (a) Continuous laser case Ti-C-RM2 using the adapted EEM indicator; (b) Pulsed laser case Ti-P-RM1 using the adapted DDEM indicator.

terms of acoustic environment, thermal boundary conditions, and scan strategies. Finally, the transferability of the material-specific filter cutoff frequencies to other machine configurations remains to be demonstrated. Furthermore, while the proposed indicators are computationally lightweight and amenable to real-time implementation, the present work was performed entirely offline; real-time deployment was not demonstrated.

These results establish a transparent and reproducible foundation for acoustic process monitoring in PBF-LB/M. Future work should address the transferability of the proposed indicators to production-scale systems and multi-layer builds. The main envisioned benefit of this work is that through the proposed amplitude modulation approach, the frequency band of interest can be freely selected to be the frequency band with the highest signal to noise ratio, which will likely differ from machine to machine. In addition, future work will investigate the material-dependent differences in acoustic response, particularly the higher classification performance observed for Ti6Al4V, and evaluate the feasibility of integrating these indicators into closed-loop process control.

CRediT authorship contribution statement

Rik Vaerenberg: Writing – review & editing, Writing – original draft, Visualization, Validation, Methodology, Formal analysis, Data curation, Conceptualization. **Bey Vrancken:** Writing – review & editing, Supervision, Resources, Project administration, Funding acquisition. **Milad Hamidi Nasab:** Writing – review & editing, Writing – original draft, Visualization, Validation, Supervision, Project administration, Methodology, Investigation, Funding acquisition, Formal analysis, Data curation, Conceptualization. **Federica Marone:** Writing – review & editing, Resources. **Antti Salminen:** Writing – review & editing, Resources. **Konstantinos Gryllias:** Writing – review & editing, Supervision, Resources, Project administration, Funding acquisition. **Florian Aymanns:** Writing – review & editing, Visualization. **Ashish Ganvir:** Writing – review & editing, Resources, Funding acquisition. **Steven Van Petegem:** Writing – review & editing, Resources, Methodology, Investigation. **Yunhui Chen:** Writing – review & editing, Methodology. **Alexander Rack:** Writing – review & editing, Resources, Methodology. **Lucas Schlenger:** Writing – review & editing, Methodology, Investigation, Conceptualization. **Roland E. Logé:** Writing – review & editing, Supervision, Resources, Project administration, Funding acquisition, Conceptualization.

Declaration of Competing Interest

The authors declare that they have no known competing financial interests or personal relationships that could have appeared to influence the work reported in this paper.

Acknowledgements

The authors would like to acknowledge the Paul Scherrer Institute, Villigen, Switzerland for provision of synchrotron radiation beamtime at the TOMCAT beamline X02DA of the SLS. This research was partially supported by Flanders Make, the strategic research center for the manufacturing industry via the MUSIC SBO project.

Furthermore, Dr. Schlenger and Prof. Logé would like to acknowledge the generous support of PX Group to the LMTM laboratory and together with Dr. Van Petegem they the support of the SMARTAM project from the Strategic Focus Area Advanced Manufacturing (SFA-AM), a strategic initiative of the ETH Board, Switzerland. In addition, Dr. Van Petegem would like to acknowledge the funding from the Swiss National Science Foundation (SNSF, grant No. 193799). Prof. Ganvir acknowledges the funding support from Tenure-Track grant to Prof. Ashish Ganvir; Research Council of Finland as well as European Council for co-funded M.ERANET 2022, GREEN-BAT (2022–2025) project and Research Council of Finland funded SOLACE, 360540 (2024–2028) project. Finally, Rik Vaerenberg would like to acknowledge the FWO SBO fellowship program (project number: 1SE9325N).

Appendix A. Process parameters for experiments

Table A1
Process parameters for the re-melting (RM) passes and passes with powder (M) on 316 L stainless steel walls utilizing continuous laser mode

	Experiment ID	Nominal Laser Power (W)	Scanning Velocity (mm/s)	Line Energy (J/m)	Acq. Freq. X-ray Imaging (1/s)
316 L Stainless Steel – Continuous Laser	SS-C-RM1	58	30	1933	1e4
	SS-C-RM2	65	30	2167	1e4
	SS-C-RM3	50	30	1667	1e4
	SS-C-RM4	65	30	2167	1e4
	SS-C-RM5	60	30	2000	1e4
	SS-C-RM6	65	30	2167	1e4
	SS-C-M7	65	30	2167	1e4
	SS-C-RM8	60	30	2000	1e4
	SS-C-RM9	50	30	1667	1e4
	SS-C-RM10	70	30	2333	1e4
	SS-C-RM11	65	30	2167	1e4
	SS-C-M12	70	30	2333	1e4
	SS-C-M13	60	30	2000	1e4
	SS-C-RM14	65	30	2467	1e4
	SS-C-RM15	85	30	2833	1e4
	SS-C-M16	70	30	2333	1e4
	SS-C-M17	50	30	1667	1e4
	SS-C-RM18	60	30	2000	1e4
	SS-C-RM19	65	30	2167	1e4
	SS-C-M20	60	30	2000	1e4
	SS-C-RM21	175	30	5833	1e5
	SS-C-RM22	175	30	5833	1e5
	SS-C-RM23	100	30	3333	1e5
	SS-C-RM24	175	30	5833	1e5

Table A2
Process parameters for the re-melting (RM) passes on 316 L stainless steel walls utilizing pulsed laser mode. The scan lines which are carried over from [2] are marked with an asterisk

	Experiment ID	Nominal Laser Power (W)	Scanning Velocity (mm/s)	Line Energy (J/m)	Acq. Freq. X-ray Imaging (1/s)
316 L Stainless Steel – Pulsed Laser	SS-P-RM1*	200	40	5000	1e4
	SS-P-RM2*	186	40	4650	1e4
	SS-P-RM3*	200	30	6667	1e4
	SS-P-RM4	365	100	3650	1e4
	SS-P-RM5	186	40	4650	1e4
	SS-P-RM6	186	40	4650	1e4
	SS-P-RM7*	186	40	4650	1e4
	SS-P-RM8	186	40	4650	1e4
	SS-P-RM9	186	40	4650	1e4
	SS-P-RM10*	186	40	4650	1e4
	SS-P-RM11*	186	40	4650	1e4
	SS-P-RM12	186	40	4650	1e4
	SS-P-RM13	186	40	4650	1e4
	SS-P-RM14	150	30	5000	1e4

Table A3
Process parameters for the re-melting (RM) passes and passes with powder (M) on Ti6Al4V walls utilizing continuous (C) and pulsed laser (P) modes

	Experiment ID	Nominal Laser Power (W)	Scanning Velocity (mm/s)	Line Energy (J/m)	Acq. Freq. X-ray Imaging (1/s)
C	Ti-C-RM1	70	50	1400	1.5e4
	Ti-C-RM2	65	40	1625	1.5e4
	Ti-C-RM3	65	40	1625	1.5e4
	Ti-C-RM4	55	40	1375	1e4
	Ti-C-M5	60	40	1500	1e4
P	Ti-P-RM1	155	40	3875	1.5e4
	Ti-P-RM2	150	40	3750	1.5e4

Appendix B. Sensitivity analysis

As the sensitivity analysis requires to see the influence of a multitude of variables across multiple datasets, a single performance metric was chosen in order to perform it which was the Matthews correlation coefficient (MCC) [56], albeit the metric is not as interpretable as other metrics, it is considered a metric with little bias due to class imbalance and has the added benefit of using all of the information in the confusion matrix [57].

Note that for almost all filter values, the performance is quite robust, with the performance either being very robust against the change in filter values or a wide range of filter values showing a near-optimal performance. One exception is the high pass filter for the unstable keyhole detection in the LDEM, which showed good performance at a high value and a low value, with a dip in the middle.

Effect of the denoising

The effect of the denoising can be seen by comparing the results of Table 2 with the results shown in Table B1, which shows a small performance drop across most cases which is most pronounced in the continuous laser case. Interestingly, the LDEM is not that affected by the denoising, likely due to the pulsed laser allowing for better inherent signal and noise separation.

Table B1
Performance of the proposed melting regime prediction indicators across all the considered scan tracks for 316 L steel and Ti6Al4V, considering both continuous and pulsed laser modes without denoising. The cases where the performance drops without denoising are underlined.Performance reported in binary F1-score which captures the classification between conduction mode and keyhole mode. The classification between unstable and stable keyholes indicated by Keyhole stability F1. The ternary classification task is evaluated using the weighted average F1 score. As there was only a single scan track of Ti6Al4V with pulsed laser exhibiting keyholes, these results were obtained without cross validated threshold setting and are indicated in cursive

		316 L			Ti6Al4V		
		Conduction-keyhole F1	**Keyhole stability F1**	**Ternary weighted F1**	**Conduction-keyhole F1**	**Keyhole stability F1**	**Ternary weighted F1**
Pulsed	**FEB**	95.40	72.06	91.57	*99.22*	*49.15*	*96.70*
	DDEM	97.65	90.29	96.44	*99.24*	*70.79*	*97.97*
	LDEM	96.84	76.54	93.11	*99.39*	*71.54*	*98.08*
Continuous	**FEB**	94.56	77.13	89.10	99.17	76.08	96.76
	EEM	94.56	78.21	89.40	99.16	80.83	97.15

Effect of window length

While the window length was chosen in accordance with previous work [2], the performance can also be evaluated on smaller windows as shown in Table B2. While the performance is generally retained at 0.5 ms windows, a decrease can be seen at 0.2 ms windows (except for the Ti6Al4V pulsed laser case which is likely due to the fact that there was no cross validation scheme possible here).

Table B2
Effect of window length as captured by the MCC. As there was only a single scan track of Ti6Al4V with pulsed laser exhibiting keyholes, these results were obtained without cross validated threshold setting and are indicated in cursive

		316 L			Ti6Al4V		
		0.2 ms	**0.5 ms**	**1.25 ms**	**0.2 ms**	**0.5 ms**	**1.25 ms**
Pulsed	**FEB**	0.851	0.867	0.876	*0.940*	*0.944*	*0.940*
	DDEM	0.892	0.918	0.937	*0.952*	*0.957*	*0.957*
	LDEM	0.834	0.877	0.898	*0.953*	*0.958*	*0.958*
Continuous	**FEB**	0.827	0.827	0.828	0.910	0.923	0.922
	EEM	0.829	0.831	0.830	0.927	0.933	0.935

316 L continuous laser filter settings

The first filter which needs to be set is the high-pass cutoff filter which is used both in the FEB and the EEM. The sensitivity to these filters is shown in Fig. B1, where one can see the optimal performance generally lies between 120 – 170 kHz cutoff with more pronounced performance drops outside of that range. Note that the actual highest performance was obtained for either 140 kHz or 160 kHz, however the middle between these peaks at 150 kHz was in the end chosen as a final value. Note as well that the proposed EEM is less sensitive to this parameter than the FEB.

For the EEM, there is another filter cutoff frequency to distinguish the high frequency oscillations from the low frequency oscillations which is shown in Fig. B2. The first thing to note is the small scale of changes in the MCC for the low pass frequency, for the high pass frequency, 40 kHz was optimal, and for simplicity, the same cutoff was chosen for the low pass.

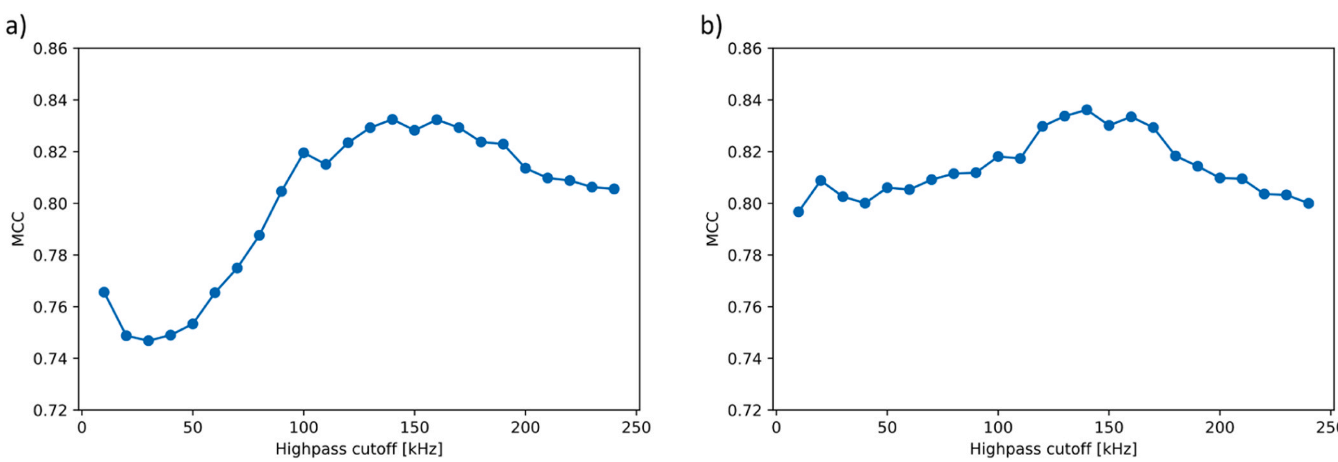

Figure B1. The effect of the initial high pass cutoff filter for 316 L for a) the FEB methodology and b) the EEM methodology

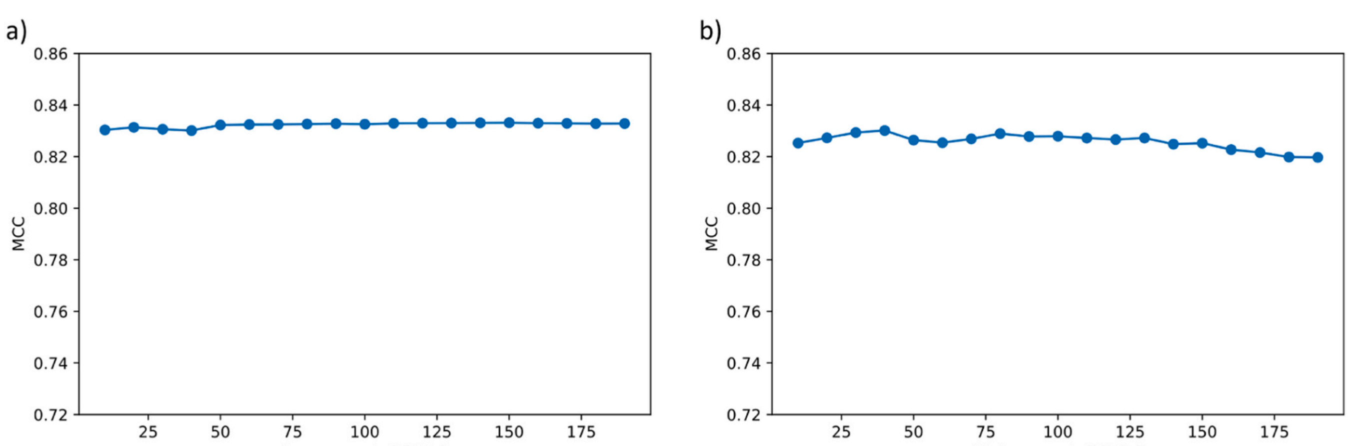

Figure B2. The effect of a) the lowpass and b) the high pass filter on the envelope for the EEM methodology on the 316 L scan lines with continuous laser

Ti6Al4V continuous laser filter settings

For the Ti6Al4V case, setting the first high pass filter was less straight forward as shown in Fig. B3. There is a clear plateau of performance in both methodologies between 90 kHz and 220 kHz, with the peak for the FEB methodology at 190 kHz and the EEM methodology at 120 kHz and a second smaller peak at 210 kHz. To balance the performance between the two methodologies the value of 210 kHz was chosen.

Similar to the 316 L case, the lowpass filter on the envelope did only have a minimal effect on the MCC as shown in Fig. B4. Therefore, the cutoff frequency was chosen at 80 kHz for both the high pass and low pass.

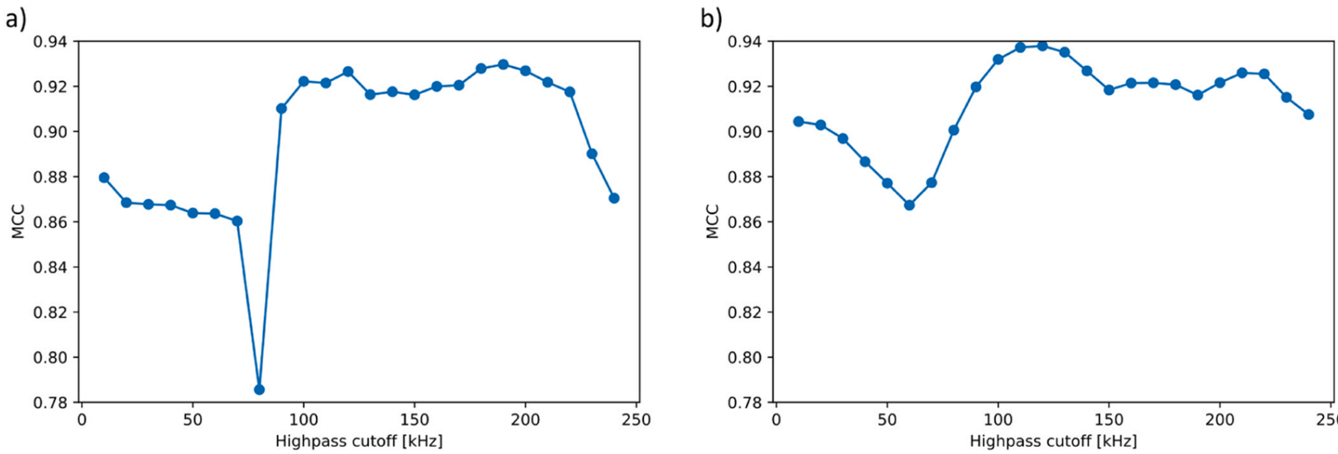

Figure B3. The effect of the initial high pass cutoff filter for Ti6Al4V for a) the FEB methodology and b) the EEM methodology

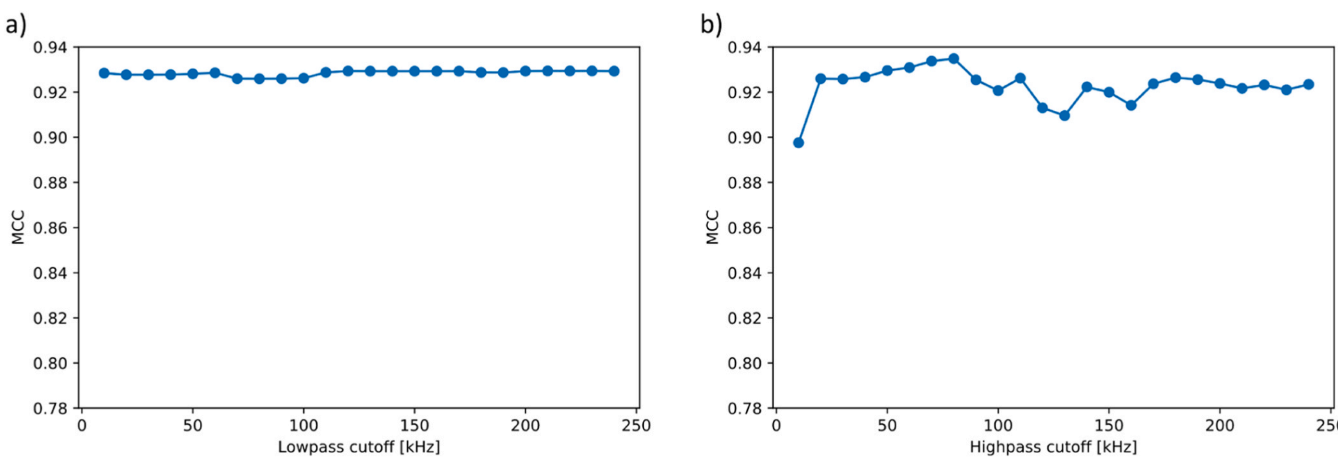

Figure B4. The effect of a) the lowpass and b) the high pass filter on the envelope for the EEM methodology on the Ti6Al4V scan lines with continuous laser

4.1. 316 L pulsed laser filter settings

For the pulsed laser case the FEB only had a single low pass filter positioned just below the pulse laser frequency due to the fact that the pulse laser frequency content was not correlated with the synchrotron images.

For the DDEM methodology, there are two filters which can be changed: the bandwidth of filtering around the 250 kHz pulse laser frequency for the keyhole detection, and the high pass filter on the second envelope for the unstable keyhole detection. Note that the bandwidth of the bandpass filter applied on the first envelope for the unstable keyhole classification was chosen as wide as possible without including the DC component or higher harmonics of the pulse laser frequency. The result of this sensitivity analysis can be seen in Fig. B5, where the optimal values are 50 kHz bandwidth and a high pass cutoff frequency of 30 kHz.

For the LDEM methodology there are three free parameters to consider: the initial high pass filter on the envelope, the lowpass filter for keyhole detection and the high pass filter for unstable keyhole classification. The result of this sensitivity analysis is shown in Fig. B6 where it is clear that the most sensitive one is the high pass filter for the classification of unstable keyholes with optimality near the extremes.

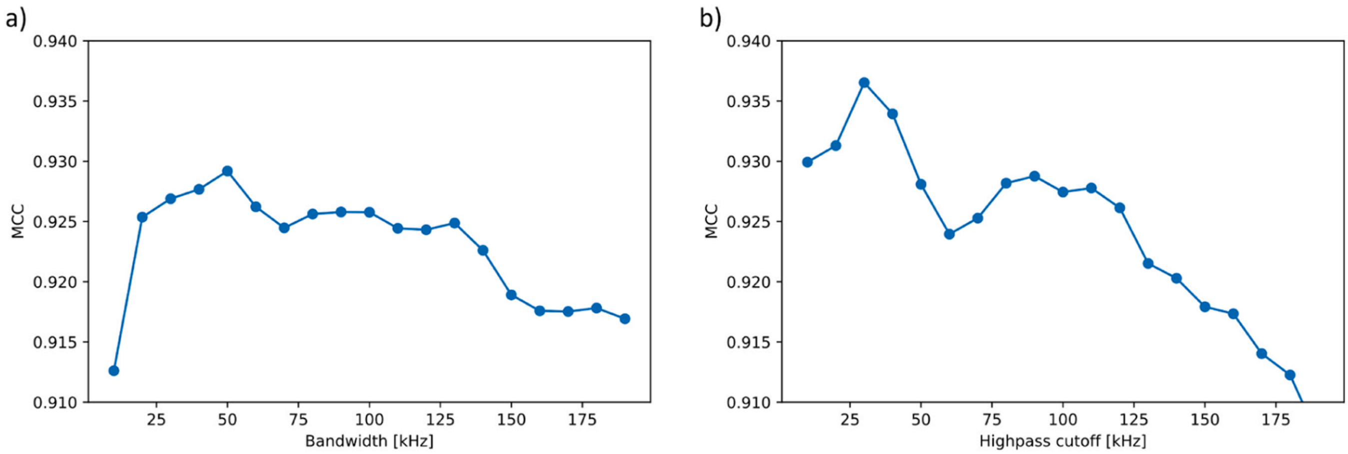

Figure B5. Sensitivity of the DDEM parameters on the 316 L case a) the bandwidth of the bandpass filter on the envelope for keyhole detection and b) the high pass cutoff frequency on the second envelope for the unstable keyhole classification

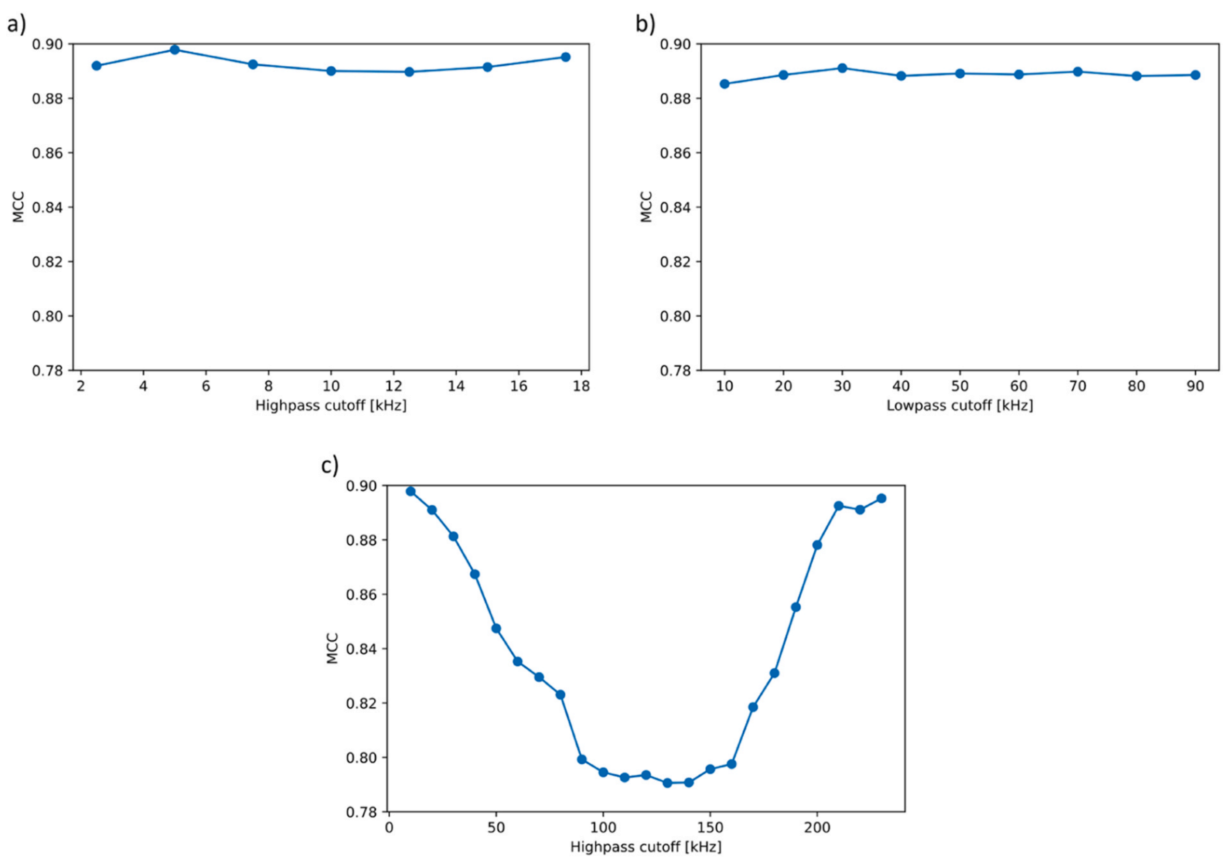

Figure B6. Sensitivity of the LDEM parameters on the 316 L case a) the cutoff of the initial high pass filter b) the cutoff of the lowpass filter for the keyhole detection c) the high pass cutoff for the unstable keyhole detection

Ti6Al4V pulsed laser filter settings

The same filter values need to be set in the Ti6Al4V pulsed case. However, note here that this can only be done using a single scan track.

First of all, the same filter values for the DDEM are investigated and reported in Fig. B7, where the optimal values are 440 kHz bandwidth for the bandpass filter and 140 kHz as the cutoff frequency for the high pass filter.

Similarly, the sensitivity to the filter values for the LDEM methodology on the Ti6Al4V case is reported in Fig. B8, where the optimal values are 7.5 kHz for the initial high pass filter on the envelope, 150 kHz for the lowpass filter for the keyhole detection and 230 kHz for the high pass filter for the unstable keyhole classification.

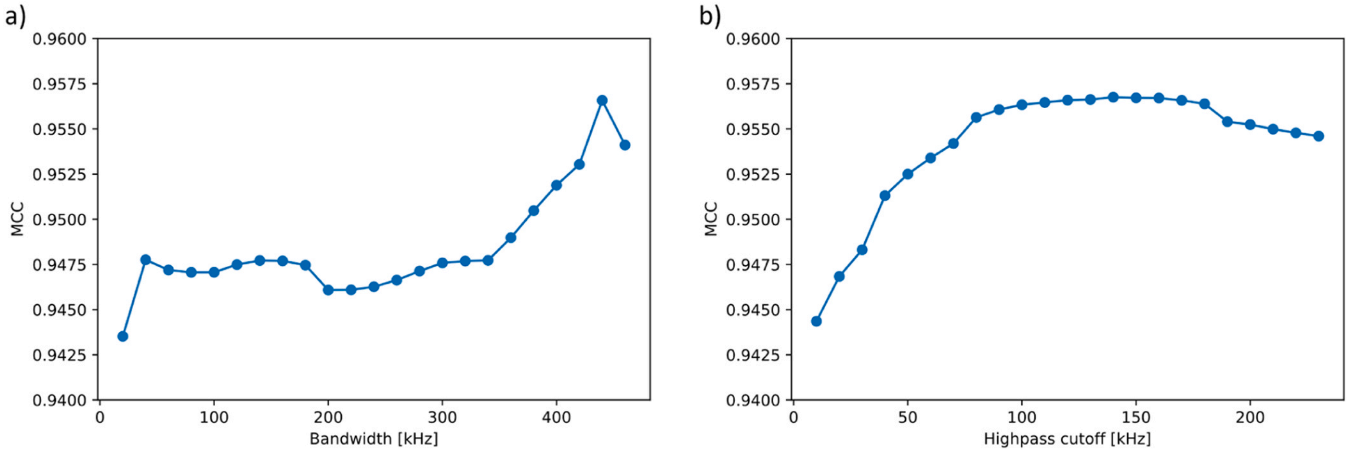

Figure B7. Sensitivity of the DDEM parameters on the Ti6Al4V case a) the bandwidth of the bandpass filter on the envelope for keyhole detection and b) the high pass cutoff frequency on the second envelope for the unstable keyhole classification

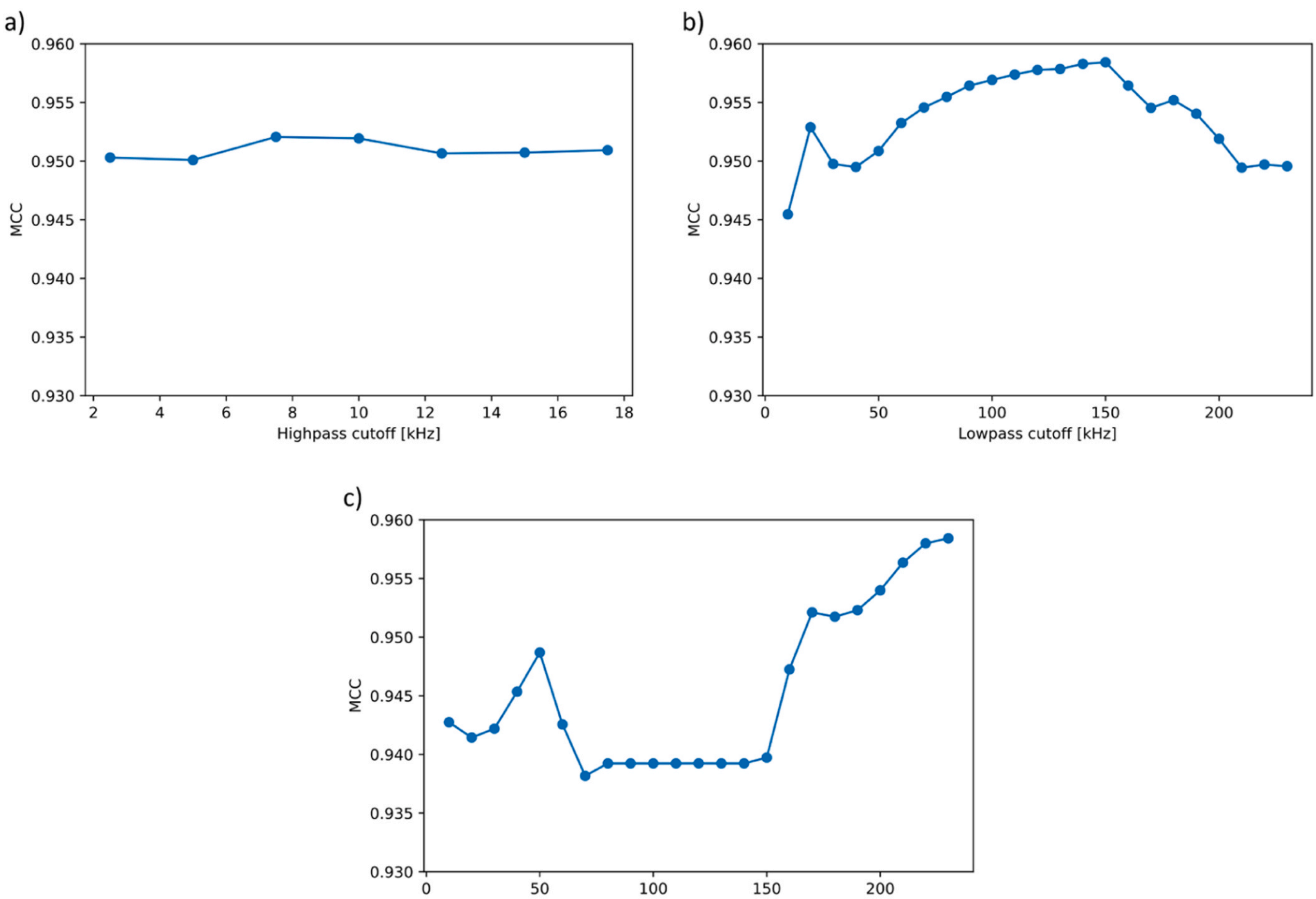

Figure B8. Sensitivity of the LDEM parameters on the Ti6Al4V case a) the cutoff of the initial high pass filter b) the cutoff of the lowpass filter for the keyhole detection c) the high pass cutoff for the unstable keyhole detection

Appendix C. Confusion matrices and balanced accuracy

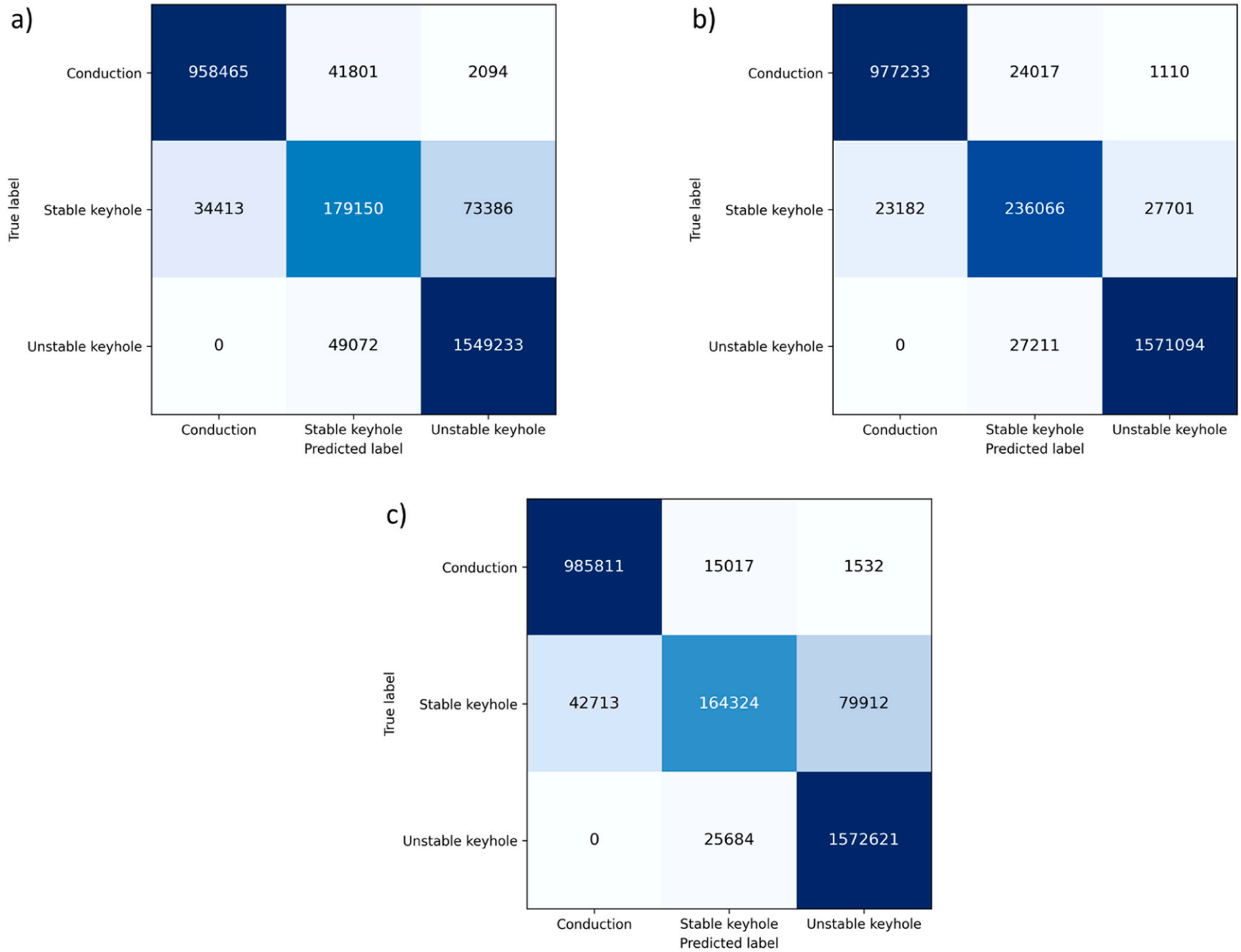

Figure C1. Confusion matrix for the 316 L pulsed case using a) the FEB b) the DDEM and c) the LDEM

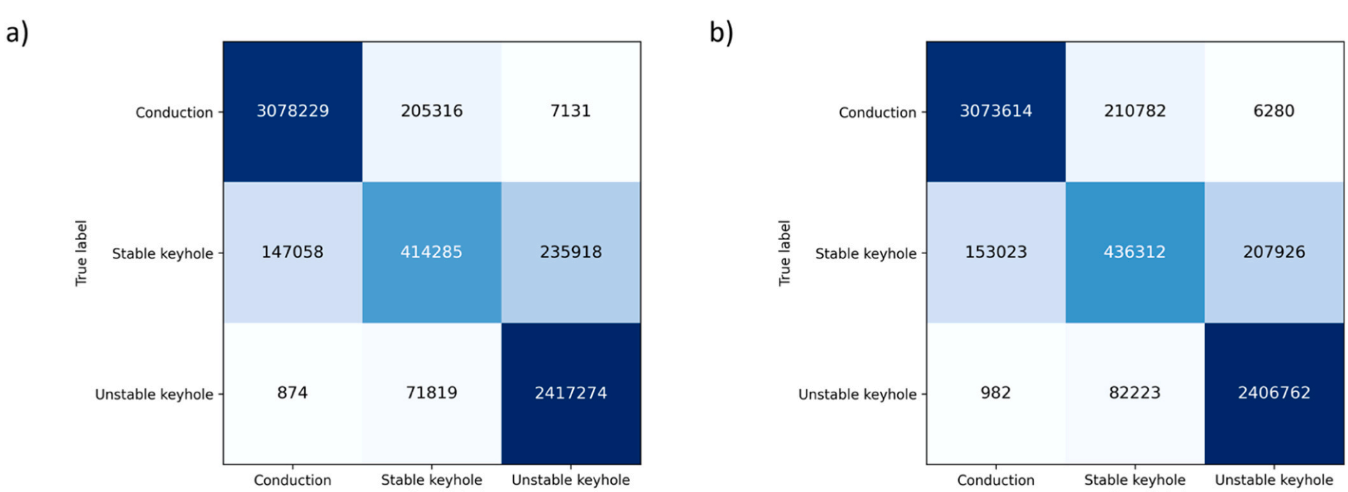

Figure C2. Confusion matrix for the 316 L continuous laser case using a) the FEB b) the EEM

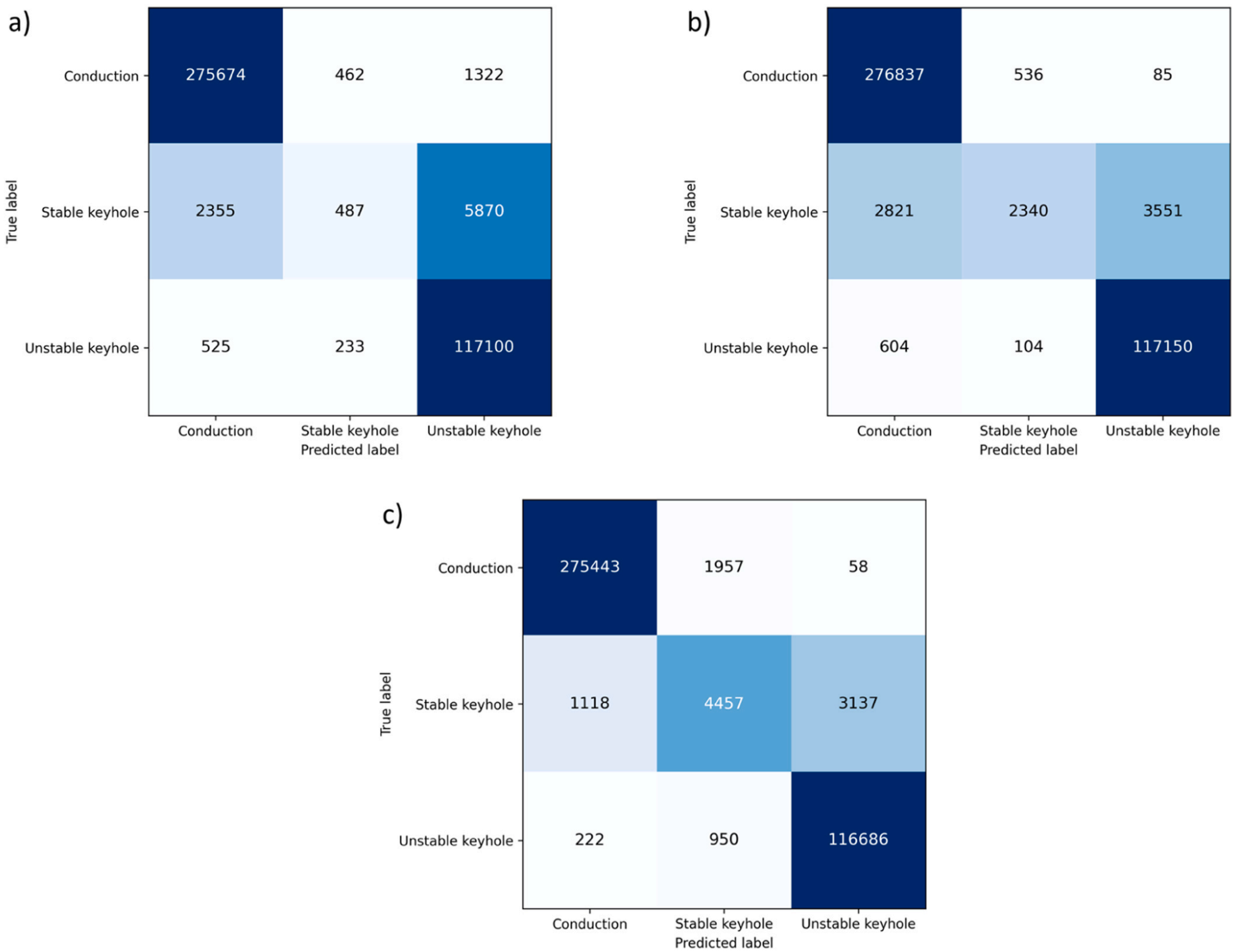

Figure C3. Confusion matrix for the Ti6Al4V pulsed case using a) the FEB b) the DDEM and c) the LDEM

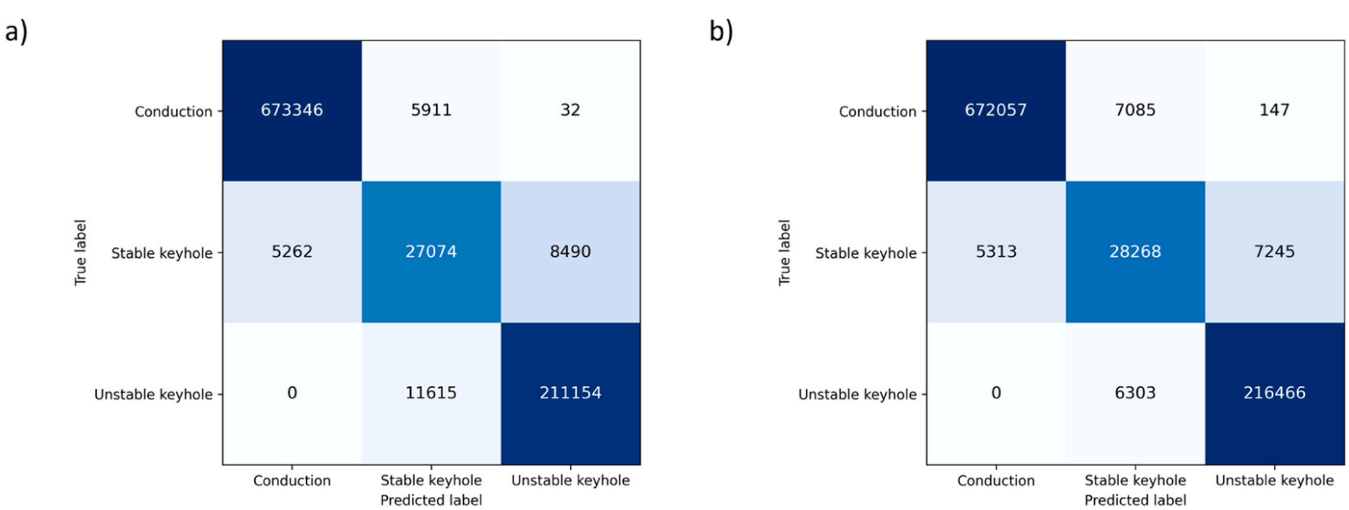

Figure C4. Confusion matrix for the Ti6Al4V continuous laser case using a) the FEB b) the EEM

Table C1
Performance of the indicators as measured by balanced accuracy (in %). As there was only a single scan track of Ti6Al4V with pulsed laser exhibiting keyholes, these results were obtained without cross validated threshold setting and are indicated in cursive. The results are computed for the conduction vs keyhole task, the task of classifying keyholes as stable or unstable and the ternary classification task where a segment needs to be classified as conduction, stable keyhole or unstable keyhole

		316 L			Ti6Al4V		
		Conduction vs keyhole	**Stable vs unstable keyhole**	**Ternary classification**	**Conduction vs keyhole**	**Stable vs unstable keyhole**	**Ternary classification**
Pulsed	**FEB**	95.54	85.68	84.99	*98.42*	*65.99*	*68.10*
	DDEM	98.03	94.32	92.69	*99.06*	*79.33*	*75.34*
	LDEM	96.04	85.27	84.67	*98.94*	*81.59*	*83.15*
Continuous	**FEB**	95.57	83.74	80.86	96.80	87.00	86.74
	EEM	95.71	85.29	81.60	98.07	89.71	88.45

Appendix D. Root mean square error linear depth prediction

Table D1
Root mean square error of a linear regressor predicting the depth

		FEB	DDEM	LDEM
Pulsed	**SS-P-RM14**	41.7 µm	31.2 µm	37.7 µm
	Ti-P-RM1	21.0 µm	18.9 µm	21.1 µm
		FEB	**EEM**	
Continuous	**SS-C-M17**	16.8 µm	16.8 µm	
	Ti-C-RM2	25.1 µm	25.1 µm	

Data availability

Data will be made available on request.

References

[1] M. Armstrong, H. Mehrabi, N. Naveed, An overview of modern metal additive manufacturing technology, J. Manuf. Process. 84 (2022) 1001–1029, https://doi.org/10.1016/j.jmapro.2022.10.060.

[2] M. Hamidi Nasab, G. Masinelli, C. de Formanoir, L. Schlenger, S. Van Petegem, R. Esmaeilzadeh, K. Wasmer, A. Ganvir, A. Salminen, F. Aymanns, Harmonizing sound and light: X-ray imaging unveils acoustic signatures of stochastic inter-regime instabilities during laser melting, Nat. Commun. 14 (2023) 8008, https://doi.org/10.1038/s41467-023-43371-3.

[3] Q. Chen, Y. Zhao, S. Strayer, Y. Zhao, K. Aoyagi, Y. Koizumi, A. Chiba, W. Xiong, A. C. To, Elucidating the effect of preheating temperature on melt pool morphology variation in Inconel 718 laser powder bed fusion via simulation and experiment, Addit. Manuf. 37 (2021) 101642, https://doi.org/10.1016/j.addma.2020.101642.

[4] Q. Guo, M. Qu, L.I. Escano, S.M.H. Hojjatzadeh, Z. Young, K. Fezzaa, L. Chen, Revealing melt flow instabilities in laser powder bed fusion additive manufacturing of aluminum alloy via in-situ high-speed X-ray imaging, Int. J. Mach. Tools Manuf. 175 (2022) 103861, https://doi.org/10.1016/j.ijmachtools.2022.103861.

[5] A.A. Martin, N.P. Calta, S.A. Khairallah, J. Wang, P.J. Depond, A.Y. Fong, V. Thampy, G.M. Guss, A.M. Kiss, K.H. Stone, Dynamics of pore formation during laser powder bed fusion additive manufacturing, Nat. Commun. 10 (2019) 1987, https://doi.org/10.1038/s41467-019-10009-2.

[6] C. Druzgalski, A. Ashby, G. Guss, W. King, T.T. Roehling, M.J. Matthews, Process optimization of complex geometries using feed forward control for laser powder bed fusion additive manufacturing, Addit. Manuf. 34 (2020) 101169, https://doi.org/10.1016/j.addma.2020.101169.

[7] A. Ashby, G. Guss, R.K. Ganeriwala, A.A. Martin, P.J. DePond, D.J. Deane, M. J. Matthews, C.L. Druzgalski, Thermal history and high-speed optical imaging of overhang structures during laser powder bed fusion: a computational and experimental analysis, Addit. Manuf. 53 (2022) 102669, https://doi.org/10.1016/j.addma.2022.102669.

[8] Y. Huang, T.G. Fleming, S.J. Clark, S. Marussi, K. Fezzaa, J. Thiyagalingam, C.L. A. Leung, P.D. Lee, Keyhole fluctuation and pore formation mechanisms during laser powder bed fusion additive manufacturing, Nat. Commun. 13 (2022) 1170, https://doi.org/10.1038/s41467-022-28694-x.

[9] R. Cunningham, C. Zhao, N. Parab, C. Kantzos, J. Pauza, K. Fezzaa, T. Sun, A. D. Rollett, Keyhole threshold and morphology in laser melting revealed by ultrahigh-speed x-ray imaging, Science 363 (2019) 849–852, https://doi.org/10.1126/science.aav4687.

[10] M. Wei, W.J. Ding, G. Vastola, Y.-W. Zhang, Quantitative study on the dynamics of melt pool and keyhole and their controlling factors in metal laser melting, Addit. Manuf. 54 (2022) 102779, https://doi.org/10.1016/j.addma.2022.102779.

[11] M. Bayat, A. Thanki, S. Mohanty, A. Witvrouw, S. Yang, J. Thorborg, N.S. Tiedje, J. H. Hattel, Keyhole-induced porosities in Laser-based Powder Bed Fusion (L-PBF) of Ti6Al4V: High-fidelity modelling and experimental validation, Addit. Manuf. 30 (2019) 100835, https://doi.org/10.1016/j.addma.2019.100835.

[12] P.S. Cook, A.B. Murphy, Simulation of melt pool behaviour during additive manufacturing: underlying physics and progress, Addit. Manuf. 31 (2020) 100909, https://doi.org/10.1016/j.addma.2019.100909.

[13] C. Zhao, N.D. Parab, X. Li, K. Fezzaa, W. Tan, A.D. Rollett, T. Sun, Critical instability at moving keyhole tip generates porosity in laser melting, Science 370 (2020) 1080–1086, https://doi.org/10.1126/science.abd1587.

[14] L. Wang, Y. Zhang, H.Y. Chia, W. Yan, Mechanism of keyhole pore formation in metal additive manufacturing, NPJ Comput. Mater. 8 (2022) 22, https://doi.org/10.1038/s41524-022-00699-6.

[15] M.H. Nasab, S. Romano, D. Gastaldi, S. Beretta, M. Vedani, Combined effect of surface anomalies and volumetric defects on fatigue assessment of AlSi7Mg fabricated via laser powder bed fusion, Addit. Manuf. 34 (2020) 100918, https://doi.org/10.1016/j.addma.2019.100918.

[16] L.R. Goossens, B. Van Hooreweder, A virtual sensing approach for monitoring melt-pool dimensions using high speed coaxial imaging during laser powder bed fusion of metals, Addit. Manuf. 40 (2021) 101923, https://doi.org/10.1016/j.addma.2021.101923.

[17] C.K.P. Vallabh, X. Zhao, Melt pool temperature measurement and monitoring during laser powder bed fusion based additive manufacturing via single-camera two-wavelength imaging pyrometry (STWIP), J. Manuf. Process. 79 (2022) 486–500, https://doi.org/10.1016/j.jmapro.2022.04.058.

[18] A.R. Ziefuss, P. Gabriel, R. Streubel, M. Nachev, B. Sures, F. Eibl, S. Barcikowski, In-situ composition analysis during laser powder bed fusion of Nd-Fe-based feedstock using machine-integrated optical emission spectroscopy, Mater. Des. 244 (2024) 113211, https://doi.org/10.1016/j.matdes.2024.113211.

[19] I. Bitharas, N. Parab, C. Zhao, T. Sun, A. Rollett, A. Moore, The interplay between vapour, liquid, and solid phases in laser powder bed fusion, Nat. Commun. 13 (2022) 2959, https://doi.org/10.1038/s41467-022-30667-z.

[20] J. Yuan, Q. Guo, S.J. Clark, Escano LI, A. Nabaa, M. Qu, J. Huang, Q. Li, A. J. Román, T.A. Osswald, others. Revealing mechanisms of processing defect mitigation in laser powder bed fusion via shaped beams using high-speed X-ray imaging, Int. J. Mach. Tools Manuf. 204 (2025) 104232, https://doi.org/10.1016/j.ijmachtools.2024.104232.

[21] D.Y. Kononenko, V. Nikonova, M. Seleznev, J. van den Brink, D. Chernyavsky, An in situ crack detection approach in additive manufacturing based on acoustic emission and machine learning, Addit. Manuf. Lett. 5 (2023) 100130, https://doi.org/10.1016/j.addlet.2023.100130.

[22] M. Seleznev, T. Gustmann, J.M. Friebel, U.A. Peuker, U. Kühn, J.K. Hufenbach, H. Biermann, A. Weidner, situ detection of cracks during laser powder bed fusion using acoustic emission monitoring, Addit. Manuf. Lett. 3 (2022) 100099, https://doi.org/10.1016/j.addlet.2022.100099.

[23] J.R. Tempelman, A.J. Wachtor, E.B. Flynn, P.J. Depond, J.-B. Forien, G.M. Guss, N. P. Calta, M.J. Matthews, Detection of keyhole pore formations in laser powder-bed

fusion using acoustic process monitoring measurements, Addit. Manuf. 55 (2022) 102735, https://doi.org/10.1016/j.addma.2022.102735.

[24] K. Gutknecht, M. Cloots, R. Sommerhuber, K. Wegener, Mutual comparison of acoustic, pyrometric and thermographic laser powder bed fusion monitoring, Mater. Des. 210 (2021) 110036, https://doi.org/10.1016/j.matdes.2021.110036.

[25] J.R. Tempelman, A.J. Wachtor, E.B. Flynn, P.J. Depond, J.-B. Forien, G.M. Guss, N. P. Calta, M.J. Matthews, Sensor fusion of pyrometry and acoustic measurements for localized keyhole pore identification in laser powder bed fusion, J. Mater. Process. Technol. 308 (2022) 117656, https://doi.org/10.1016/j.jmatprotec.2022.117656.

[26] S. Gorgannejad, A.A. Martin, J.W. Nicolino, M. Strantza, G.M. Guss, S. Khairallah, J.-B. Forien, V. Thampy, S. Liu, P. Quan, others. Localized keyhole pore prediction during laser powder bed fusion via multimodal process monitoring and X-ray radiography, Addit. Manuf. 78 (2023) 103810, https://doi.org/10.1016/j.addma.2023.103810.

[27] T. DebRoy, T. Mukherjee, H. Wei, J. Elmer, J. Milewski, Metallurgy, mechanistic models and machine learning in metal printing, Nat. Rev. Mater. 6 (2021) 48–68, https://doi.org/10.1038/s41578-020-00236-1.

[28] V. Pandiyan, R. Drissi-Daoudi, S. Shevchik, G. Masinelli, T. Le-Quang, R. Logé, K. Wasmer, Semi-supervised Monitoring of Laser powder bed fusion process based on acoustic emissions, Virtual Phys. Prototyp. 16 (2021) 481–497, https://doi.org/10.1080/17452759.2021.1966166.

[29] J. Li, J. Hu, Q. Zhou, Y. Zhang, Transfer learning-based quality monitoring of laser powder bed fusion across materials, Expert. Syst. Appl. 252 (2024) 124150, https://doi.org/10.1016/j.eswa.2024.124150.

[30] R. Drissi-Daoudi, G. Masinelli, C. de Formanoir, K. Wasmer, J. Jhabvala, R.E. Logé, Acoustic emission for the prediction of processing regimes in Laser Powder Bed Fusion, and the generation of processing maps, Addit. Manuf. 67 (2023) 103484, https://doi.org/10.1016/j.addma.2023.103484.

[31] G.D. Goh, S.L. Sing, W.Y. Yeong, A review on machine learning in 3D printing: applications, potential, and challenges, Artif. Intell. Rev. 54 (2021) 63–94, https://doi.org/10.1007/s10462-020-09876-9.

[32] S. Lapuschkin, S. Wäldchen, A. Binder, G. Montavon, W. Samek, K.-R. Müller, Unmasking Clever Hans predictors and assessing what machines really learn, Nat. Commun. 10 (2019) 1096, https://doi.org/10.1038/s41467-019-08987-4.

[33] N. Eschner, L. Weiser, B. Häfner, G. Lanza, Classification of specimen density in laser powder bed fusion (L-PBF) using in-process structure-borne acoustic process emissions, Addit. Manuf. 34 (2020) 101324, https://doi.org/10.1016/j.addma.2020.101324.

[34] L. Galiègue, F. Briffod, K. Ito, H. Masuo, M. Watanabe, T. Shiraiwa, M. Enoki, Acoustic emission monitoring reveals keyhole formation and evolution, Sci. Rep. 15 (2025) 43243, https://doi.org/10.1038/s41598-025-27232-1.

[35] Y. Sun, S. Gorgannejad, A. Martin, J. Nicolino, M. Strantza, J.-B. Forien, V. Thampy, S. Liu, P. Quan, C.J. Tassone, Direct mechanistic connection between acoustic signals and melt pool morphology during laser powder bed fusion, Appl. Phys. Lett. 125 (2024).

[36] Liu H., Naghibzadeh S.K., Ren Z., Zhang Y., Shao J., Clark S.J., Fezzaa K., Zeng X., Gao L., Yan W., others. Aeroacoustic signatures reveal fast transient dynamics of vapor-jet-driven cavity oscillations in metallic additive manufacturing. arXiv Preprint arXiv:260300789 2026.

[37] E. Ruckh, R. Lambert-Garcia, S. Hocine, A.C. Getley, C. Iantaffi, A. Bhatt, M. Fitzpatrick, S. Marussi, A. Farndell, T. Schubert, others. Process mapping of Ti-6Al-4V laser powder bed fusion using in situ high-speed synchrotron x-ray imaging, Addit. Manuf. (2025) 105007, https://doi.org/10.1016/j.addma.2025.105007.

[38] S.M.H. Hojjatzadeh, N.D. Parab, Q. Guo, M. Qu, L. Xiong, C. Zhao, L.I. Escano, K. Fezzaa, W. Everhart, T. Sun, others. Direct observation of pore formation mechanisms during LPBF additive manufacturing process and high energy density laser welding, Int. J. Mach. Tools Manuf. 153 (2020) 103555, https://doi.org/10.1016/j.ijmachtools.2020.103555.

[39] T. Florian, K. Schricker, C. Zenz, A. Otto, L. Schmidt, C. Diegel, H. Friedmann, M. Seibold, P. Hellwig, F. Fröhlich, others. Combining in situ synchrotron X-ray imaging and multiphysics simulation to reveal pore formation dynamics in laser welding of copper, Int. J. Mach. Tools Manuf. 204 (2025) 104224, https://doi.org/10.1016/j.ijmachtools.2024.104224.

[40] S. Hocine, S. Van Petegem, U. Frommherz, G. Tinti, N. Casati, D. Grolimund, H. Van Swygenhoven, A miniaturized selective laser melting device for operando X-ray diffraction studies, Addit. Manuf. 34 (2020) 101194.

[41] Z. Gan, O.L. Kafka, N. Parab, C. Zhao, L. Fang, O. Heinonen, T. Sun, W.K. Liu, Universal scaling laws of keyhole stability and porosity in 3D printing of metals, Nat. Commun. 12 (2021) 2379, https://doi.org/10.1038/s41467-021-22704-0.

[42] J. Ahlers, D. Althviz Moré, O. Amsalem, A. Anderson, G. Bokota, P. Boone, J. Bragantini, G. Buckley, A. Burt, M. Bussonnier, napari: a multi-dimensional image viewer for Python, Zenodo (2023), https://doi.org/10.5281/zenodo.3555620.

[43] S.A. Khairallah, T. Sun, B.J. Simonds, Onset of periodic oscillations as a precursor of a transition to pore-generating turbulence in laser melting, Addit. Manuf. Lett. 1 (2021) 100002, https://doi.org/10.1016/j.addlet.2021.100002.

[44] J. Liu, P. Wen, Metal vaporization and its influence during laser powder bed fusion process, Mater. Des. 215 (2022) 110505.

[45] Z. Ren, L. Gao, S.J. Clark, K. Fezzaa, P. Shevchenko, A. Choi, W. Everhart, A. D. Rollett, L. Chen, T. Sun, Machine learning–aided real-time detection of keyhole pore generation in laser powder bed fusion, Science 379 (2023) 89–94, https://doi.org/10.1126/science.add4667.

[46] J.C. Whitaker, M.H. Kryder, J.F. Shackelford, V.K. Tripathi, G. DeSantis, E. D. Fabricius, M.D. Yacoub, M. Pecht, C. Sankaran, Y. Ephraim, The electronics handbook, Crc Press, 2018.

[47] V. Pandiyan, R. Drissi-Daoudi, S. Shevchik, G. Masinelli, R. Logé, K. Wasmer, Analysis of time, frequency and time-frequency domain features from acoustic emissions during Laser Powder-Bed fusion process, Procedia Cirp 94 (2020) 392–397, https://doi.org/10.1016/j.procir.2020.09.152.

[48] L. Chen, X. Yao, C. Tan, W. He, J. Su, F. Weng, Y. Chew, N.P.H. Ng, S.K. Moon, In-situ crack and keyhole pore detection in laser directed energy deposition through acoustic signal and deep learning, Addit. Manuf. 69 (2023) 103547, https://doi.org/10.1016/j.addma.2023.103547.

[49] P. Scalart, Speech enhancement based on a priori signal to noise estimation, 2, IEEE, 1996, pp. 629–632, https://doi.org/10.1109/ICASSP.1996.543199.

[50] P. Welch, The use of fast Fourier transform for the estimation of power spectra: a method based on time averaging over short, modified periodograms, IEEE Trans. Audio Electro 15 (1967) 70–73, https://doi.org/10.1109/TAU.1967.1161901.

[51] S. Butterworth, On the theory of filter amplifiers, Wirel. Eng. 7 (1930) 536–541.

[52] F. Gustafsson, Determining the initial states in forward-backward filtering, IEEE Trans. Signal. Process. 44 (2002) 988–992, https://doi.org/10.1109/78.492552.

[53] M. Feldman, Hilbert transform in vibration analysis, Mech. Syst. Signal. Process. 25 (2011) 735–802, https://doi.org/10.1016/j.ymssp.2010.07.018.

[54] B.J. Simonds, J. Sowards, J. Hadler, E. Pfeif, B. Wilthan, J. Tanner, C. Harris, P. Williams, J. Lehman, Time-resolved absorptance and melt pool dynamics during intense laser irradiation of a metal, Phys. Rev. Appl. 10 (2018) 044061, https://doi.org/10.1103/PhysRevApplied.10.044061.

[55] L. Caprio, A.G. Demir, B. Previtali, Observing molten pool surface oscillations during keyhole processing in laser powder bed fusion as a novel method to estimate the penetration depth, Addit. Manuf. 36 (2020) 101470, https://doi.org/10.1016/j.addma.2020.101470.

[56] B.W. Matthews, Comparison of the predicted and observed secondary structure of T4 phage lysozyme, Biochim. Et. Biophys. Acta (BBA)-Protein Struct. 405 (1975) 442–451, https://doi.org/10.1016/0005-2795(75)90109-9.

[57] A. Luque, A. Carrasco, A. Martín, A. de Las Heras, The impact of class imbalance in classification performance metrics based on the binary confusion matrix, Pattern Recognit. 91 (2019) 216–231, https://doi.org/10.1016/j.patcog.2019.02.023.